



## RESEARCH ARTICLE

10.1002/2014JC009807

## The critical role of stratification in submarine channels: Implications for channelization and long runout of flows

R. M. Dorrell<sup>1</sup>, S. E. Darby<sup>2</sup>, J. Peakall<sup>1</sup>, E. J. Sumner<sup>3,4</sup>, D. R. Parsons<sup>5</sup>, and R. B. Wynn<sup>6</sup>

## Key Points:

- Vertical stratification of density-driven flows enhances runout length
- Existing empirical models under predict flow stratification
- Stratification may explain formation of sandy lobes at the end of submarine fans

## Correspondence to:

R. M. Dorrell,  
r.m.dorrell@leeds.ac.uk

## Citation:

Dorrell, R. M., S. E. Darby, J. Peakall, E. J. Sumner, D. R. Parsons, and R. B. Wynn (2014), The critical role of stratification in submarine channels: Implications for channelization and long runout of flows, *J. Geophys. Res. Oceans*, 119, 2620–2641, doi:10.1002/2014JC009807.

Received 10 JAN 2014

Accepted 31 MAR 2014

Accepted article online 3 APR 2014

Published online 22 APR 2014

<sup>1</sup>Department of Earth and Environment, University of Leeds, Leeds, UK, <sup>2</sup>Department of Geography and Environment, University of Southampton, Southampton, UK, <sup>3</sup>Monterey Aquarium Research Institute, Moss Landing, California, USA, <sup>4</sup>Department of Ocean and Earth Science, University of Southampton, Southampton, UK, <sup>5</sup>Department of Geography, Earth, and Environment Sciences, University of Hull, Hull, UK, <sup>6</sup>National Oceanography Centre, University of Southampton Waterfront Campus, Southampton, UK

**Abstract** Channelized submarine gravity currents travel remarkable distances, transporting sediment to the distal reaches of submarine fans. However, the mechanisms by which flows can be sustained over these distances remain enigmatic. In this paper we consider two shallow water models the first assumes the flow is unstratified whilst the second uses empirical models to describe vertical stratification, which effects depth averaged mass and momentum transfer. The importance of stratification is elucidated through comparison of modeled flow dynamics. It is found that the vertically stratified model shows the best fit to field data from a channelized field-scale gravity current in the Black Sea. Moreover, the stratified flow is confined by the channel to a much greater degree than the flow in the unstratified model. However, both models fail to accurately represent flow dynamics in the distal end of the system, suggesting current empirical stratification models require improvement to accurately describe field-scale gravity currents. It also highlights the limitations of weakly stratified small-scale experiments in describing field-scale processes. The results suggest that in real-world systems stratification is likely to enable maintenance of velocity and discharge within the channel, thus facilitating sediment suspension over distances of hundreds of kilometers on low seafloor gradients. This explains how flows can travel remarkable distances and transport their sediment to the distal parts of submarine fans.

## 1. Introduction

Submarine density currents often form channelized flows that can travel for thousands of kilometers, transporting sediment from the coastal shelf into the deep ocean [Damuth and Kumar, 1975; Chough and Hesse, 1980; Hesse et al., 1987; Khripounoff et al., 2003]. However, the dynamics of channelized submarine flows remain poorly understood, and in particular the long runout length of such flows remains enigmatic [Vangriesheim et al., 2009]. Many modeling approaches to turbidity currents assume an absence of stratification, and such approaches are referred to as depth-averaged models [Parker et al., 1986; Das et al., 2004; Parsons et al., 2009], yet it is known that the vertical structure of density-driven flows is both nonuniform and an important control on flow dynamics [Stacey and Bowen, 1988a; Peakall et al., 2000a; Abad et al., 2011]. Such evidence is provided by previous conceptual [Hiscott et al., 1997; Peakall et al., 2000a, 2001], experimental [Amy et al., 2005; Felix et al., 2005; Islam and Imran, 2010; Sequeiros et al., 2010], theoretical [Stacey and Bowen, 1988a, 1988b; Mulder et al., 1997; Felix, 2002; Abad et al., 2011; Dorrell et al., 2013a], and field based studies [Arnott, 2007; Migeon et al., 2012; Sumner et al., 2013, 2014], which have shown the influence of stratification on many aspects of density-driven flow dynamics. The variation of flow density with flow depth can be seen to control the rate of erosion and deposition at the bed, as well as entrainment of ambient fluid; in addition, the density gradient can affect the autosuspension limit above which material is permanently carried in suspension [Stacey and Bowen, 1988a, 1988b]. As flow density drives flow velocity, vertical stratification can lead to longitudinal stratification of evolving flows [Amy et al., 2005]. Moreover, the structure of the vertical variation of both flow density and velocity has been shown to control secondary flow orientation in submarine meander bends [Abad et al., 2011; Dorrell et al., 2013a; Sumner et al., 2014].

Current three-dimensional flow models have been used to investigate the behavior of secondary flow cells in meandering submarine channels [see e.g., Kassem and Imran, 2004; Giorgio Serchi et al., 2011; Ezz and Imran, 2014] and in system scale studies detailing the runout on single turbidity current events [see e.g.,

This is an open access article under the terms of the Creative Commons Attribution License, which permits use, distribution and reproduction in any medium, provided the original work is properly cited.

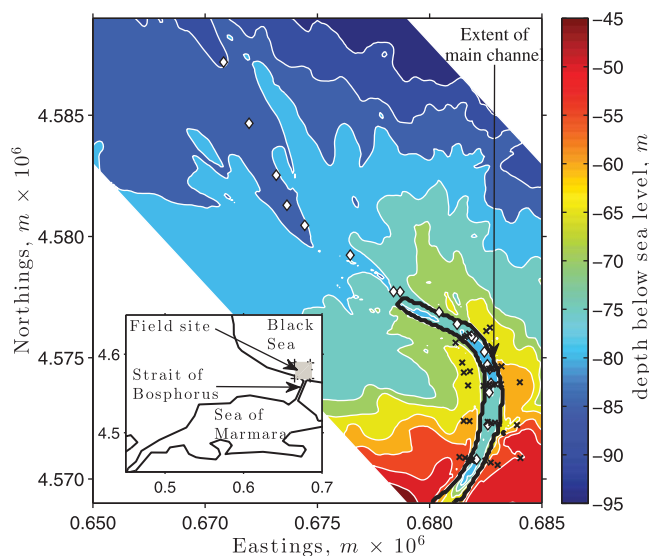


**Figure 1.** Bathymetry of the submarine canyon-fan system field site as plotted in the Universal Transverse Mercator (UTM) coordinate system. Mean flow direction is northward, through a curved channel exiting on to a smoother submarine plain. The extent of this main channel is denoted by a black contour outline. The inset shows the location of the field site at the exit of the Strait of Bosphorus in the S.W. Black Sea, adjacent to the Sea of Marmara in the Eastern Mediterranean Sea. Diamonds denote CTD cast locations along the thalweg of the channel whilst crosses denote grab sample locations taken by the *RV Koca Piri Reis*, May 2010.

Abd El-Gawad *et al.*, 2012]. However, although such models incorporate flow stratification implicitly an explicit discussion of the effect of vertical stratification on flow dynamics has not previously been made. Moreover, whilst three-dimensional models of field-scale density currents are based on the Reynolds-Averaged Navier-Stokes equations, recent research has shown that such an approach poorly captures the downstream flow evolution, where stratification induced turbulence dampening is poorly captured [Yeh *et al.*, 2013].

However, the effects of stratification are likely crucial to the evolution of the dynamics of density-driven flows. This is because vertical variation in the flow density and velocity fields affects the advective transport rates of mass, momentum and energy [Parker

*et al.*, 1986; Sequeiros *et al.*, 2010]. The dynamics of density-driven flows are controlled by their excess density relative to their ambient surroundings; therefore it is essential that models accurately describe such transport processes.

Neglecting sediment entrainment, in this paper we extend the “three-equation” depth-averaged shallow water model of Parker *et al.* [1986], which conserves mass and momentum transport of the flow, and mass of material transported by the flow, to incorporate recent empirical research on the vertical shape factors of gravity-driven flows [Islam and Imran, 2010; Sequeiros *et al.*, 2010; Abad *et al.*, 2011]. We compare this stratified flow model to the classical, unstratified, flow model [see e.g., Parker *et al.*, 1986; Das *et al.*, 2004; Zeng and Lowe, 2006; Parsons *et al.*, 2009; Hu *et al.*, 2012; Castro Díaz *et al.*, 2013], in order to elucidate the broader influence of stratification on flow interactions with topography and flow runout length.

In general deep-sea turbidity currents have proven difficult to measure, and thus directly investigate, due to their inaccessible location and infrequent occurrence, which is compounded by present sea-level high-stand [Sumner *et al.*, 2014]. However, the relatively shallow depths of the Black Sea shelf channel system and the quasi-continuous nature of the associated gravity current [Parsons *et al.*, 2010; Sumner *et al.*, 2013, 2014], provides a rare opportunity to study the dynamics of a saline-driven density current over complex topography (Figure 1). The detailed field data gathered from the Black Sea therefore allows an examination of the validity of theoretical models to describe submarine density-driven flow dynamics. The reduced complexity of the depth-averaged shallow water model employed in this study allows us to investigate the importance of key physical processes: namely the effect of stratification on depth averaged mass and momentum transfer and the resultant impact on flow dynamics. This approach allows us to explicitly examine the influence of stratification on flow dynamics within three-dimensional bend flow for the first time. The analogous nature of saline and particulate-driven density currents allows us to assess and discuss the probable controls on flow runout length in turbidity currents.

## 2. Hydrodynamic Model

The shallow water model used here to describe flow dynamics assumes that the vertical length scale, as characterized by the flow depth  $h$ , is small in comparison to typical horizontal length scales,  $L$ . The condition

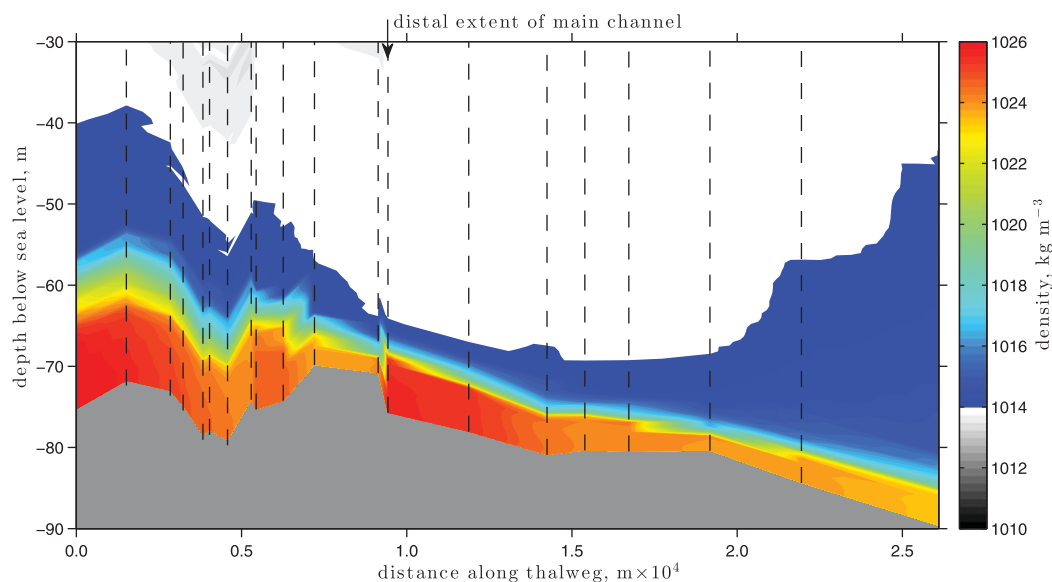


**Figure 2.** Flow stratification along the thalweg of the Black Sea channelized submarine density current plotted in Figure 1. Ambient flow salinity of the upper 40m of the Black Sea is assumed to be  $\sim 18.5$  ppt [Latif et al., 1991; Stanev et al., 2004], equivalent to a density of  $\sim 1014 \text{ kg m}^{-3}$ . Dashed lines denote CTD measurements see Figure 1.

that the aspect ratio  $\delta = h/L \ll 1$  implies that vertical flow velocities are negligible in comparison to horizontal flow velocities. Thus, a necessary constraint of shallow water models is that the bed gradient in the direction of mean flow is small. Curvature of the flow and/or large bed gradients normal to the direction of mean flow can induce comparably large secondary flow [Huijts et al., 2006; Keevil et al., 2006, 2007; Wei et al., 2013], however here these effects are here assumed to be negligible. Therefore, here the condition  $\delta \ll 1$  is assumed, see Appendix B2, implying that the pressure field is hydrostatic [see e.g., Parker et al., 1986; Tan, 1992]. The hydrostatic pressure field assumption allows the shallow water equations to be reduced to a two-dimensional depth averaged model, ideal for efficiently modeling flow hydrodynamics over complex topography.

Herein we assume that channelized density-driven submarine flow is stratified and composed of a dense core, overlain by a dilute mixing layer in which the density of the flow tends toward the density of the ambient fluid, as justified with reference to direct field observations of a channelized density current in the South West Black Sea (see Figure 2 and Appendix B) [Ünlülata et al., 1990; Latif et al., 1991; Özsoy et al., 2001; Parsons et al., 2010; Sumner et al., 2014]. Such stratification of the flow results in additional weighting terms which describe the variation of flow acceleration, mass transport and hydrostatic pressure from the classical form of the unstratified depth averaged shallow water model [see e.g., Parker et al., 1986; Hogg and Pritchard, 2004; Sequeiros et al., 2010].

### 2.1. A Shallow Water Model of Density-Driven Flows

The shallow water model is derived by depth averaging the Reynolds Averaged Navier-Stokes equations, resultant temporally averaged effects of flow turbulence are here closed using empirical models [Dyer and Soulsby, 1988; Begnudelli et al., 2010]. The Black Sea Shelf exchange flow is assumed to be saline driven, and thus it is assumed that transportation, deposition and erosion of particulate material is of negligible importance. Further, it is assumed that flow velocity and diffusive terms vanish at the flow bed and as depth tends to infinity. From these assumptions the conservation of fluid mass may be expressed as

$$\frac{\partial h}{\partial t} + \frac{\partial}{\partial x} h\bar{u} + \frac{\partial}{\partial y} h\bar{v} = E\|\bar{u}\|, \quad (1)$$

where  $h$  denotes flow depth, overbar notation denotes the depth average value of a flow parameter, the vector  $[u, v, w]$  describes the flow velocity field in the Cartesian frame of reference  $[x, y, z]$ ,  $\|\bar{u}\|$  describes the summed horizontal velocity  $\|\bar{u}\| = \sqrt{\bar{u}^2 + \bar{v}^2}$ , and  $E$  describes the rate of entrainment of ambient fluid into the flow (see Table 1) [Ellison and Turner, 1959; Parker et al., 1987]. In the absence of net entrainment of

**Table 1.** Parameters and Hydrodynamic Closures Used in the Shallow Water Model

Parameter	Closure	Description	Reference
$\delta$	$\frac{h}{L} \approx \frac{w}{ u }$	Flow aspect ratio	Tan [1992]
$Fr_d$	$\frac{ u }{\sqrt{g(\frac{\rho_s}{\rho_w}-1)\phi}}$	Densimetric Froude number	Tan [1992]
$E$	$\frac{0.075}{\sqrt{1+718Fr_d^{4.8}}}$	Ambient fluid entrainment rate	Parker et al. [1987]
$\bar{K}$	$\kappa u_* \frac{h}{6}$	Eddy diffusivity	Dyer and Soulsby [1988]
$u_*$	$\sqrt{\frac{ \bar{\tau} }{\rho_w}}$	Friction velocity	Soulsby [1997]
$k_s$	$2.5d$	Nikoradze roughness	Soulsby [1997]
$z_0$	$\frac{k_s}{30} (1 - \exp(-\frac{\kappa_s u_*}{27v})) + \frac{v}{9u_*}$	Bed roughness height	Christoffersen and Jonsson [1985]

material carried within the flow, the excess density of the flow compared to the ambient fluid, as modeled by the concentration of solute (or particulate) material transported by the flow, is

$$\frac{\partial}{\partial t} h\bar{\phi} + \frac{\partial}{\partial x} h(\bar{\phi}u + \overline{D_{px}}) + \frac{\partial}{\partial y} h(\bar{\phi}v + \overline{D_{py}}) = 0, \tag{2}$$

where  $\bar{\phi}$  is a dimensionless measure of the excess density of the flow [Dorrell et al., 2013a] (or equivalently the concentration of particulate material transported by the flow). Diffusion of material transported by the flow,  $D_{pi}$ , is modeled using a simplified empirical form [Imran et al., 2004; Dorrell and Hogg, 2012],

$$\overline{D_{px}} = -\bar{K} \frac{\partial}{\partial x} \bar{\phi}, \quad \overline{D_{py}} = -\bar{K} \frac{\partial}{\partial y} \bar{\phi}. \tag{3}$$

Here  $\bar{K}$ , the eddy diffusivity coefficient, is defined in terms of the eddy viscosity using the turbulent Schmidt number,  $\sigma_t$ , such that  $\bar{K} = \nu_t / \sigma_t$  [Imran et al., 2004; Begnudelli et al., 2010; Abd El-Gawad et al., 2012]. Since the net entrainment of sediment into the flow is assumed to be negligible, the problem of ignition of the “three-equation” gravity current model is negated [Parker et al., 1987]. As discussed by Begnudelli et al. [2010] an algebraic description of the eddy viscosity, see Table 1, forms an attractive balance between numerical efficiency and model complexity, and is the approach used herein. Further, here we set the turbulent Schmidt number equal to unity,  $\sigma_t = 1$  [Begnudelli et al., 2010; Abd El-Gawad et al., 2012] such that eddy diffusivity is equivalent to the eddy viscosity. The magnitude of eddy diffusivity (or equivalent eddy viscosity) which parameterizes diffusive effects arising through flow turbulence, may be expressed in terms of the bed friction velocity, see Table 1 and Dyer and Soulsby [1988].

Integrating the conservation of momentum equation in the vertical plane the shallow water approximation of the flow is seen to result in a hydrostatic pressure field,  $P$ , of the form

$$\bar{P} = \rho_w g' h \int_0^\infty \int_\eta^\infty \phi d\eta' d\eta \equiv \rho_w g' h \int_0^\infty \eta \phi d\eta, \tag{4}$$

where  $\eta = (z - \psi) / h$ . In a similar fashion, the shallow water equations describing the conservation of momentum in the horizontal plane are

$$\frac{\partial h\bar{u}}{\partial t} + \frac{\partial}{\partial x} h \left( \bar{u}^2 + \frac{\bar{P}}{\rho_w} \right) + \frac{\partial}{\partial y} h\bar{u}v = -g'h\bar{\phi} \frac{\partial \psi}{\partial x} + fh\bar{v} - \frac{\partial}{\partial x} \frac{h\bar{\tau}_{xx}}{\rho_w} - \frac{\partial}{\partial y} \frac{h\bar{\tau}_{xy}}{\rho_w} - \frac{\bar{\tau}_{xz}}{\rho_w}, \tag{5}$$

$$\frac{\partial h\bar{v}}{\partial t} + \frac{\partial}{\partial x} h\bar{u}v + \frac{\partial}{\partial y} h \left( \bar{v}^2 + \frac{\bar{P}}{\rho_w} \right) = -g'h\bar{\phi} \frac{\partial \psi}{\partial y} - fh\bar{u} - \frac{\partial}{\partial x} \frac{h\bar{\tau}_{yx}}{\rho_w} - \frac{\partial}{\partial y} \frac{h\bar{\tau}_{yy}}{\rho_w} - \frac{\bar{\tau}_{yz}}{\rho_w}, \tag{6}$$

where  $P$  denotes the pressure field,  $\psi$  the bed depth and  $\rho_w$  the fluid density. The density of material transported by the flow  $\rho_s$ , and thus the reduced gravity of the flow,  $g'$ , is given by the specific gravity,  $g$ , multiplied by  $\rho_s / \rho_w - 1$ . The total flow density,  $\rho_f$ , is therefore

$$\rho_f = (1 - \phi)\rho_w + \phi\rho_s. \tag{7}$$

For a saline flow, such as the one we model herein,  $\rho_s \approx 1760\text{kgm}^{-3}$  [Chernetsky et al., 2010] and the density of the ambient fluid, i.e., the Black Sea (see Appendix B), is  $\rho_w = 1014\text{kgm}^{-3}$  [Latif et al., 1991]. The Coriolis force,  $f = 2\omega\sin\alpha$ , where  $\omega = 7.3 \times 10^{-5}\text{s}^{-1}$  is the Earth's rate of rotation and  $\alpha$  the latitude, is derived such that on the Cartesian plane the  $x$  axis is oriented due East and  $y$  due North. The summed viscous and Reynolds' stress terms are modeled following the standard form as

$$\overline{\tau_{xx}} = -\rho_w 2(v + \bar{v}_t) \frac{\partial \bar{u}}{\partial x}, \quad \overline{\tau_{xy}} = \overline{\tau_{yx}} = -\rho_w (v + \bar{v}_t) \left( \frac{\partial \bar{v}}{\partial x} + \frac{\partial \bar{u}}{\partial y} \right), \quad \overline{\tau_{yy}} = -\rho_w 2(v + \bar{v}_t) \frac{\partial \bar{v}}{\partial y}, \tag{8}$$

where  $\nu$  is the kinematic viscosity of the fluid [see e.g., Imran et al., 2004; Begnudelli et al., 2010; Abd El-Gawad et al., 2012]. The depth integrated frictional stresses,  $\tau_{xz}$  and  $\tau_{yz}$ , are given in terms of a Chezy drag coefficient,  $C_z$ , [see e.g., Hutter and Nohguchi, 1990; Garcia and Parker, 1993; Wu, 2004]

$$\overline{\tau_{xz}} = \rho_w \frac{1}{C_z^2} \bar{u} \|\bar{u}\|, \quad \overline{\tau_{yz}} = \rho_w \frac{1}{C_z^2} \bar{v} \|\bar{u}\|, \tag{9}$$

The total frictional shear stress,  $\|\tau\|$ , may thus be defined as

$$\|\tau\| = \sqrt{\overline{\tau_{xz}^2} + \overline{\tau_{yz}^2}} = \rho_w \frac{1}{C_z^2} \|\bar{u}\|^2. \tag{10}$$

### 2.2. Vertical Stratification of the Flow, Drag, and Resultant Shape Factors

Classical analysis of flow dynamics using shallow water theory is based on the assumption that the flow velocity and distribution of material transported by the flow are uniform within the flow, and zero outside it. This implies that the depth integrated terms, which consist of multiple variables, in the shallow water model are equivalent to the product of the depth integrated values of their component parts [Parker et al., 1986; Sequeiros et al., 2010]. However, the assumption of a vertically uniform flow, often referred to as a "top-hat" model (see e.g., section 2) [Parker et al., 1986], is inappropriate for describing the dynamics of stratified channelized flows [Abad et al., 2011; Sumner et al., 2014]. Flow stratification is readily generated by the entrainment of ambient fluid [see e.g., Peakall et al., 2000a; Sequeiros et al., 2010; Abad et al., 2011] or through the balance of gravitational settling and turbulent diffusion, which results in greater mass concentration near the bed [see e.g., Stacey and Bowen, 1988a, 1988b; Hiscott et al., 1997; Peakall et al., 2000a]. Further, vertical stratification of the flow density strongly affects the vertical structure of the flow velocity field [Amy et al., 2005].

Thus, assuming that both the velocity and density fields (the latter being defined by the concentration of material transported by the flow) are vertically stratified we must consider the implications on the depth integrated values of the terms

$$\overline{u^2}, \quad \overline{uv}, \quad \overline{v^2}, \quad \overline{u\phi}, \quad \overline{v\phi}, \quad \text{and} \quad \overline{P}. \tag{11}$$

To do so we assume that the vertical structure of these parameters may be readily described using empirical structure functions, where

$$u = \frac{\zeta_1(\eta)}{\int_0^\infty \zeta_1 d\eta} \bar{u}(x, y) \quad \text{and} \quad v = \frac{\zeta_1(\eta)}{\int_0^\infty \zeta_1 d\eta} \bar{v}(x, y), \tag{12}$$

see for example, Parker et al. [1986], such that  $\|u\| = \zeta_1 \sqrt{\bar{u}^2 + \bar{v}^2} / \int_0^\infty \zeta_1 d\eta$ , and

$$\phi = \frac{\zeta_2(\eta)}{\int_0^\infty \zeta_2 d\eta} \bar{\phi}. \tag{13}$$

In Table 2 the shape factors, given the above structure functions, are presented for unstratified and stratified flow models. Assuming a stratified flow it is seen that additional (in comparison to an unstratified flow)

**Table 2.** Shape Factors for Unstratified and Stratified Shallow Water Models

Shape factor	Depth Integrated Variable	
	Unstratified	Stratified
$\bar{u} = \int_0^\infty u d\eta$	$\bar{u}$	$\bar{u}$
$\overline{uv} = \int_0^\infty uv d\eta$	$\bar{u}\bar{v}$	$W_{u^2}\bar{u}\bar{v}$ , where $W_{u^2} = \int_0^\infty \zeta_1^2 d\eta$
$\overline{u^2} = \int_0^\infty u^2 d\eta$	$\bar{u}^2$	$W_{u^2}\bar{u}^2$ , where $W_{u^2} = \int_0^\infty \zeta_1^2 d\eta$
$\bar{\phi} = \int_0^\infty \phi d\eta$	$\bar{\phi}$	$\bar{\phi}$
$\overline{u\phi} = \int_0^\infty u\phi d\eta$	$\bar{u}\bar{\phi}$	$W_{u\phi}\bar{u}\bar{\phi}$ , where $W_{u\phi} = \int_0^\infty \zeta_1 \zeta_2 d\eta$
$2\bar{P} = 2\rho_w g' h \int_0^\infty \int_\eta^\infty \phi d\eta' d\eta$	$\rho_w g' h \bar{\phi}$	$\rho_w g' h W_P \bar{\phi}$ , where $W_P = 2 \int_0^\infty \eta \zeta_2 d\eta$

weighting parameters arise due to depth averaging variables in the mass, (1) and (2), and momentum conservation equations, (4) and (5).

The shallow water model (1)–(6) is therefore closed by the structure functions detailing the vertical variation in flow velocity,  $\zeta_1$ , and of material transported by the flow,  $\zeta_2$ . Outside the flow there is no material transport and thus, for  $\eta > 1$ , flow velocity and excess density are zero,  $\zeta_1 = 0$  and  $\zeta_2 = 0$  respectively; however inside the flow the vertical variation of the velocity field is described by the structure function [Abad et al., 2011],

$$\zeta_1 = \begin{cases} \frac{\chi + \eta - \frac{1}{2}\eta^2}{\chi + \eta_1 - \frac{1}{2}\eta_1^2} & \eta \leq \eta_1 \\ \frac{1 - \eta}{1 - \eta_1} & \eta_1 < \eta \leq 1 \end{cases}, \tag{14}$$

where the parameter  $\eta_1$  is the dimensionless depth of the downstream flow velocity maximum and  $\chi$  is a slip velocity parameter [Engelund, 1974]. The slip velocity parameter is defined in terms of the Chezy drag coefficient,  $C_z$ ,

$$\left(\frac{0.077}{\chi + \frac{1}{3}}\right)^2 = \frac{1}{C_z^2}, \tag{15}$$

see for example, Abad et al. [2011]. From the experimental study of Sequeiros et al. [2010], Abad et al. [2011] propose that  $\eta_1$  may be empirically related to the densimetric Froude number (see Table 1),

$$\eta_1 = 0.8 - 0.27 Fr_d \quad \text{for} \quad 0.19 \leq Fr_d \leq 2.21. \tag{16}$$

For  $\eta \leq \eta_1$  the slip velocity model closely approximates the flow velocity as commonly modeled by the log-law of the wall [Soulsby, 1997]. Thus, equating the log-law of the wall [Soulsby, 1997], to the flow velocity in the near-bed layer, (12) and (14),

$$\|u\| \frac{\zeta_1(\eta)}{\int_0^1 \zeta_1 d\eta} \approx \frac{u_*}{\kappa} \log\left(\frac{\eta h}{z_0}\right) \quad \text{for} \quad \eta \leq \eta_1, \tag{17}$$

where  $u_* = \sqrt{|\tau|/\rho_w}$  (see Table 1) is the friction velocity,  $z_0/h$  is the dimensionless roughness height above the bed, and  $\kappa = 0.41$  is von Karman's constant. Here frictional stresses at the flow–ambient fluid interface

[Kostic and Parker, 2006] are assumed negligible; the frictional drag, characterized by the Chezy drag coefficient, is therefore determined by the bed roughness. Setting  $\eta = \eta_1$  in (17), and using (10), the Chezy drag coefficient modeling the frictional drag within the flow is

$$C_z \approx \frac{\int_0^1 \zeta_1 d\eta}{\kappa} \log\left(\frac{\eta_1 h}{z_0}\right). \tag{18}$$

Given the slip velocity condition (15) and the bed roughness length, see Table 1 and Christoffersen and Jonsen [1985], (18) may be solved to implicitly yield a dynamic description of frictional drag,  $C_z$ . In this paper we use this derivation of the drag coefficient in both the unstratified and stratified flow models compared in section 3. Moreover, the derivation of  $C_z$  is assumed to hold for all  $Fr_d$  (16), although it is also assumed that  $\eta_1 \geq z_0/h$ . Further, a constraint  $\eta_1 \geq z_0/h$  is enforced such that the near bed flow velocity is always approximated by the slip velocity model in (14).

To model vertical variation of flow density, Abad et al. [2011] use a structure function of the form

$$\zeta_2 = \begin{cases} 1 & \eta \leq \eta_2 \\ \frac{1-\eta}{1-\eta_2} & \eta_2 < \eta \leq 1 \end{cases}, \tag{19}$$

which is based on the experimental data of Sequeiros et al. [2010]. In (19)  $\eta_2$  denotes the dimensionless depth below which the flow is approximately uniformly stratified. Abad et al. [2011] propose that the dimensionless depth  $\eta_2$  may also be expressed as a function of the densimetric Froude number

$$\eta_2 = \min(2.59 \exp(-2.5 Fr_d), 1) \quad \text{for} \quad 0.19 \leq Fr_d \leq 2.21. \tag{20}$$

In density-driven flows the pressure field,  $\bar{P}$ , described by the excess density of material transported by the flow, is critical to determining flow dynamics. Key to understanding the pressure field in a stratified flow is the pressure field weighting function,

$$W_p = 2 \int_0^\infty \int_\eta^\infty \zeta_2 d\eta' d\eta = 2 \int_0^\infty \eta \zeta_2 d\eta, \tag{21}$$

which implies pressure is weighted by distance above the flow bed (see Table 2). The variation of  $W_p$  as a function of densimetric Froude number is plotted in Figure 3, highlighting that as Froude number increases the depth averaged hydrostatic pressure is reduced, i.e.,  $W_p$  decreases as flow stratification is increased. This is because, as with increasing stratification, material transported by the flow is predominately found closer to the flow bed, and thus contributes less to the depth averaged pressure (21). Further, in Figure 3 the variation of the convective transport and convective acceleration weighting terms,  $W_{u\phi}$  and  $W_{u^2}$  respectively, are plotted. The convective mass transport weighting term is increased as stratification drives the flow velocity maximum toward the excess density maximum; while the convective acceleration term is increased since stratification increases the relative value of the flow velocity maximum [Dorrell et al., 2013a].

### 2.3. Stratification Effects on Channelized Flows

It is useful to discuss the effects of vertical stratification on flow dynamics. We do so to motivate the study presented in the latter half of this paper, where unstratified and stratified versions of the shallow water model are compared (see sections 3 and 4, and Appendix B). In order to elucidate the effect of vertical stratification on flow channelization, we pose a thought experiment, balancing hydrostatic and gravitational forces, discussed below.

Assuming that inertial forces are negligible in comparison to the hydrostatic and gravitational forces, i.e.,  $\bar{u} \ll g' \bar{\phi} h$ , the momentum conservation equation (5) reduces to,

$$\frac{\partial}{\partial x} \left( \frac{W_p}{2} g' \bar{\phi} h^2 \right) = -g' \bar{\phi} h \frac{\partial \psi}{\partial x}, \tag{22}$$

to leading order, where  $W_p$  is the hydrostatic pressure weighting term introduced in section 2.2. We also make the simplifying assumption that the sum of the bed and flow depth is constant,  $\psi + h = c_0$ . Substituting  $\psi = c_0 - h$  into (22) we find that

$$\frac{\partial}{\partial x} (W_p \bar{\phi}) = \left( \frac{2(1-W_p)}{h} \frac{\partial h}{\partial x} \right) \bar{\phi}. \tag{23}$$

If  $W_p = 1$  everywhere, as in classical unstratified flow models (see Table 2), it is immediately noted that (23) implies that the depth averaged flow concentration is constant

$$\bar{\phi} = c_1. \tag{24}$$

As flow density is constant, independent of topography, the flow is poorly constrained and not well channeled. However, if  $W_p < 1$ , as in a stratified flow, (23) may be solved without assuming  $\bar{\phi}$  is constant. Indeed (23) may be integrated to show that

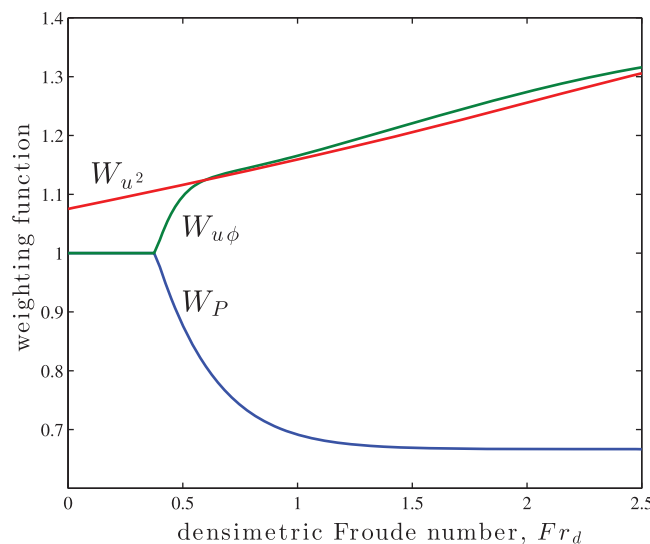
$$\bar{\phi} = c_1 h^{2\frac{1-W_p}{W_p}} = c_1 (c_0 - \psi)^{2\frac{1-W_p}{W_p}}. \tag{25}$$

Thus, assuming  $W_p$  is some constant less than unity, the flow density increases when moving toward the topographic minimum.

The principle of topographic confinement of stratified flow, for constant  $W_p < 1$ , is demonstrated in the example below. Here the depth of a channel,  $\psi$ , across a transverse section is given by

$$\psi = c_0 - c_2 \exp\left(-\frac{1}{2} \left(\frac{x-\mu}{\sigma}\right)^2\right), \tag{26}$$

where  $c_2$  is a dimensional measure of the channel depth,  $x = \mu$  describes the location of the thalweg and  $\sigma$  is a dimensional measure of the steepness of the channel. From (26) we may readily derive the flow depth,  $h$  as



$$h = c_2 \exp\left(-\frac{1}{2} \left(\frac{x-\mu}{\sigma}\right)^2\right), \tag{27}$$

and from (25) the depth averaged flow concentration,  $\bar{\phi}$ , equivalent to dimensionless flow density,

$$\bar{\phi} = c_1 \exp\left(-\frac{1-W_p}{W_p} \left(\frac{x-\mu}{\sigma}\right)^2\right), \tag{28}$$

where  $c_1$  is the depth averaged concentration at  $x = \mu$ . Figures 4a and 4b compare the distribution of flow density, derived using equation (28), for both unstratified,  $W_p = 1$  (Figure 4a), and stratified flow conditions,  $W_p < 1$

**Figure 3.** Weighting terms describing the modified hydrostatic pressure,  $W_p$  (blue curve), density flux,  $W_u \phi$  (green curve) and fluid acceleration,  $W_u^2$  (red curve) in a stratified flow as a function of densimetric Froude number. The weighting terms, as defined in Table 2, are based on the structure functions (12) and (19) proposed by *Abad et al.* [2011]. The Chezy drag coefficient is taken as  $C_z = 15$ , implying a slip coefficient of  $\chi = 0.8217$  (15).

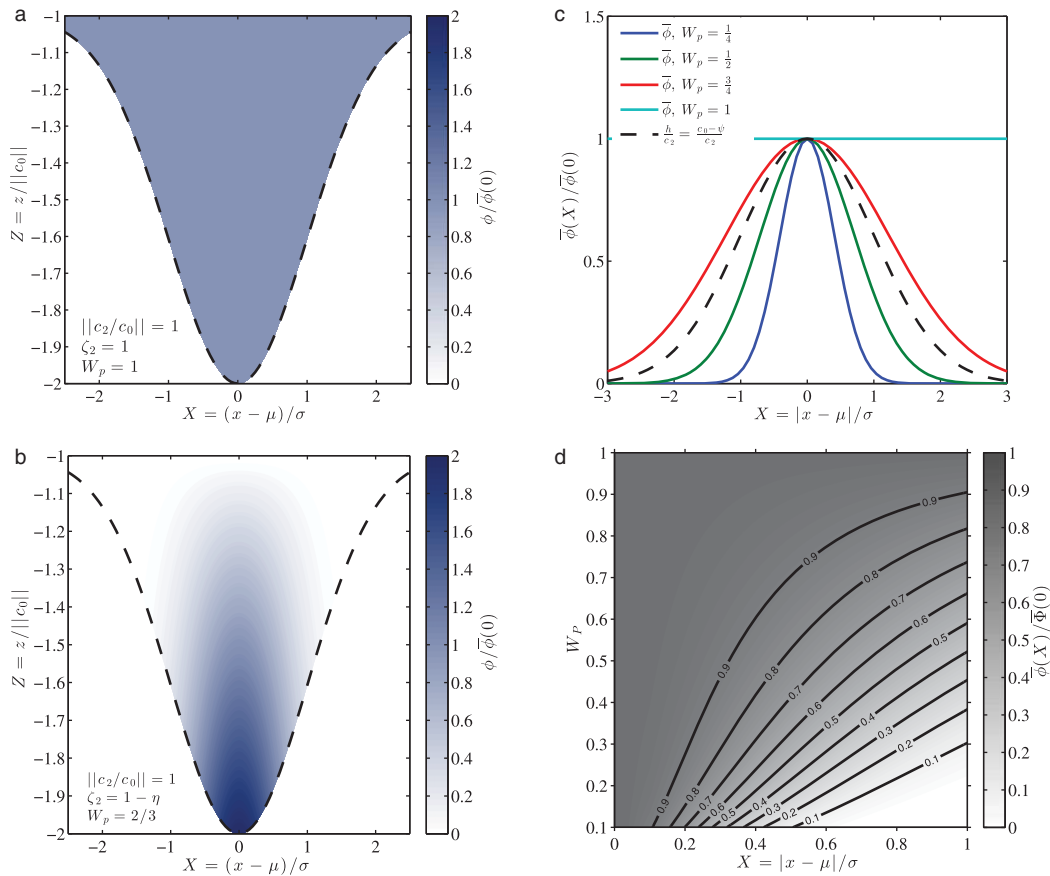


**Figure 4.** (a) Plot of the normalized concentration,  $\phi/\bar{\phi}(0)$ , for an unstratified flow where  $W_p = 1$  (28). (b) Plot of the normalized concentration for a stratified flow where  $\zeta_2 = 1 - \eta$  and  $W_p = 2/3$  (28). In Figures 4a and 4b, the dashed curve denotes the flow bed and  $X$  is a measure of dimensionless distance across channel. (c) Plot of the depth averaged normalized concentration,  $\bar{\phi}(X)/\bar{\phi}(0)$ , as a function of  $X$ , assuming an exponentially varying bed topography (26), the normalized flow depth,  $h/c_2$ , (27) is described by the dashed curve. (d) Phase space of the depth averaged normalized concentration as a function of  $W_p$  and  $X$ . Contour lines are drawn at intervals of 0.1.

(Figure 4b). It is evident that if the flow is stratified, flow density is concentrated toward the center and base of the channel, i.e., stratification is acting to increase flow channelization. The normalized depth averaged concentration at a given distance across the channel,  $X$  is plotted in Figure 4c. Here the normalized concentration is given by the depth averaged concentration divided by the maximum depth averaged density, occurring at  $X = 0$  (28). Figure 4d highlights that the density maximum occurs as  $X \rightarrow 0$ , moreover it also shows that as  $W_p \rightarrow 1$  we recover the condition of uniform flow density (24), independent of bed topography. In Figure 4d, a phase-space of the variation of normalized depth averaged concentration shows that concentration increases either as stratification decreases, i.e.,  $W_p \rightarrow 1$ , or as distance from the concentration maxima decreases, i.e.,  $X \rightarrow 0$ . These figures show that with increasing stratification the excess density of the flow is concentrated toward the centre of the channel. Whilst the flow density is concentrated in the centre of the channel, less material can be lost through overspill as there is less material near the channel banks, and thus flow duration and ultimately run out is increased.

However, the simple analysis presented above is limited to cases where  $W_p$  is assumed constant, and where inertial forces are negligible. Nevertheless, it is informative with regard to processes that we may expect to find in more complex systems, as discussed in the following section.

### 3. Density-Driven Flow Dynamics Over Complex Topography

To further elucidate the effect of stratification on submarine flow dynamics we compare numerical solutions, see Appendix A, to the unstratified and stratified shallow water model, see section 2. The performance of the models is assessed through comparison against direct observations of a saline-driven density current

in the South West Black Sea which flowed through a curved channel. Model bathymetry was therefore separated into regions of in-channel and out-of-channel flow, see Figure 1 and Appendix B. The shallow water model was integrated using a Finite Volume scheme (see Appendix A) [Delis *et al.*, 2008], with the Black Sea bathymetry represented on a rectilinear grid with cells 100 m square. Open boundary conditions were applied along all boundaries except the southern edge of the numerical domain [Causon *et al.*, 2000]. Along the southern boundary edge (located at  $4.569 \times 10^6$  m North, UTM Zone 35 T and down system of the hydraulic jump reported by Sumner *et al.* [2013]), temporally invariant input boundary conditions describing flow depth and density were prescribed to simulate field conditions. Input boundary conditions assumed the flow-ambient fluid interface to be located at a depth of 35 m below sea level and flow density to peak at the center of the thalweg at  $1020 \text{ kg m}^{-3}$  and decay exponentially to  $1015 \text{ kg m}^{-3}$  out-of-channel. Moreover, it was found that a flow velocity limiting condition ( $\|\bar{u}\| \leq 0.7 \text{ ms}^{-1}$ ) was needed at the Southern edge of the domain to prevent the model from accelerating to unphysically large flow velocities. Limiting the flow velocity may readily be seen to be equivalent to limiting the fluid flux into the domain. The value of  $\|\bar{u}\| \leq 0.7 \text{ ms}^{-1}$  was selected to match the in-channel depth-averaged flow velocity as reported by Parsons *et al.* [2010].

Based on a minimum model flow velocity observed in the numerical domain (of order  $10^{-4} \text{ ms}^{-1}$ ) and the grid cell size (of 100 m), a long time scale of flow evolution of  $10^6$  s is derived. Integrating the model over 10 times the long time scale of flow evolution, i.e.,  $10^7$  s, yielded solutions tending toward a steady state. At such time scales seasonal changes in the Strait of Bosphorus and the Black Sea may have a significant affect on the plume dynamics [Özsoy *et al.*, 1995]; however for simplicity we have assumed that the input conditions described above are constant in time. Mean changes in flow variables over the long time scale, e.g.,  $10^6$  s, of simulation time were less than 5% over the entire domain, due to the slow entrainment of ambient fluid in the distal reaches of the domain, and less than 0.05% in-channel, as defined in Figure 1. Henceforth, solutions will therefore be referred to as quasi-steady state.

### 3.1. Unstratified Flow Model Solutions

Figures 5a and 5b plot quasi-steady state shallow water model flow solutions for the Black Sea submarine channel flow, subject to the boundary conditions discussed above. Initially we assume that the flow is unstratified, such that the shape factors are approximately vertically uniform. In Figures 5a and 5b, flow solutions are plotted in the region surrounding the channel and the insets depict solutions in the distal reaches of the domain. It is important to remember that the unstratified model is constructed on the assumption that flow velocity is approximately vertically uniform, thus the velocity structure function,  $\zeta_1$  is equal to unity (see (12) and Table 2). Therefore, it is noted that in the unstratified flow model the maximum flow velocity is well described by the depth averaged flow velocity  $\|u\|_{\max} = \|\bar{u}\|$ .

The simulated flow hydrodynamics as depicted in Figure 5a are compared to ADCP-derived field data, detailing maximum flow velocity; for rationale see Appendix B1. Comparison of modeled  $\|u\|_{\max}$  with the six ADCP transects, see Appendix B1, shows that the unstratified model is poorly constrained by the channel topography. Out-of-channel model results predict large overbanking flow velocities, of order  $\sim 1 \text{ ms}^{-1}$ , initially on the left hand side at the proximal (Southern) end of the submarine channel. Toward the bend apex, predicted flow over banking is predominately located on the outer bank (right hand side), with overbank flow velocities of order  $\sim 0.5 \text{ ms}^{-1}$  driven by centrifugal forces pushing the flow away from the inner bank.

In Figure 5b the simulated flow density is compared to the depth averaged flow density derived from the CTD data, as reported in Appendix B1. Comparison of predicted versus observed flow densities further indicates that unstratified flow model solutions are poorly constrained by channel topography. Modeled density in-channel is as much as  $\sim 7 \text{ kg m}^{-3}$  smaller than observed values, especially at locations down flow of the channel bend apex. Further, by comparing Figures 5a and 5b it can be seen that as the modeled flow rapidly loses mass through over banking, the flow velocity rapidly wanes, such that modeled in-channel flow is negligible shortly after the bend apex, in contrast to observed channel flow which persists even after the bend exit.

Due to rapid loss of flow density through over banking the predicted flow density rapidly becomes up to  $\sim 3 \text{ kg m}^{-3}$  greater than that observed out-of-channel density. The modeled high density out-of-channel flow, Figure 5b, generates flow velocities that are order  $\sim 0.5 \text{ ms}^{-1}$  greater than those observed in ADCP

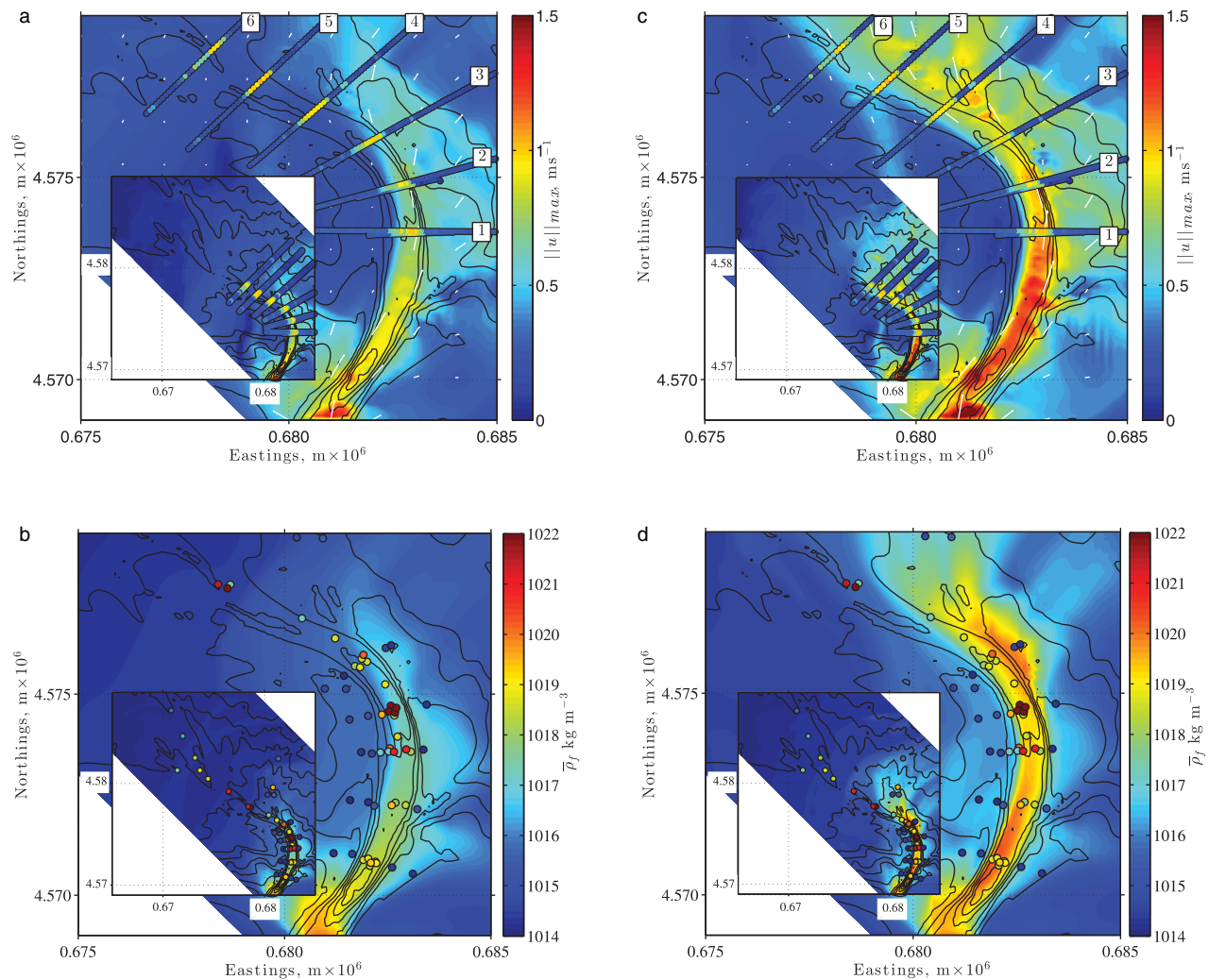


**Figure 5.** Predicted flow hydrodynamics (a) and (b) using the shallow water model with no vertical flow stratification ( $W_p \equiv 1$ ), and (c) and (d) using the structure functions of *Abad et al.* [2011], see section 2.2. Plots (a) and (c) show flow velocity maximum, and plots (b) and (d) the flow density around the extent of the main channel, see Figure 1. Insets in both plots show the flow behavior in the far field, away from the distal extent of the main channel; in Figures 5a and 5c ADCP transects are denoted 1–6, in Figures 5b and 5d CTD-derived depth averaged flow density is denoted by circles. Plots are displayed in the UTM coordinate system, zone 35 T.

transects 1–4, Figure 5a. Since the majority of the modeled flow is lost over bank, following the gradient of steepest descent (initially North-Westerly, then North-Easterly down flow of the bend apex), little material is transported past the bend exit and as such the model fails to capture flow in the distal reaches of the system, see inset Figure 5b.

### 3.2. Stratified Flow Model Solutions

Figures 5c and 5d plot alternative quasi-steady state shallow water model flow solutions for the Black Sea submarine channel flow dynamics. In these simulations it is assumed that the flow is stratified, such that the velocity field and density field are allowed to vary with flow depth (see section 2.2). In Figures 5c and 5d, the simulated flow solutions are plotted in the region surrounding the channel and the insets depict solutions in the distal reaches of the domain.

Flow solutions predicted by the stratified shallow water model, have the same generic structure as the unstratified model, Figure 5. Specifically, the flow velocity, as shown in Figure 5c is predominately in the along channel direction; although over banking, initially on the left hand side of the bend then on the right hand side at the bend apex is significantly greater than that observed, with simulated flow velocities up to

$\sim 1 \text{ ms}^{-1}$  greater than on ADCP transects 1–6. The modeled flow density shows good agreement (within  $\sim 2 \text{ kgm}^{-3}$ ) within the channel, up to and past the bend apex. However, excess over banking within the modeled results, Figure 5d, is seen to increase the out-of-channel density compared to CTD-derived data, albeit by smaller amounts than the unstratified model. Similar to the unstratified flow model, out-of-channel flow, arising from material lost through over banking, follows the gradient of steepest descent.

Moreover, it is evident that the stratified model still fails to capture the flow dynamics in the distal reaches of the channel system, see inset Figure 5b. The failure of both the unstratified and stratified models to describe flow in the distal reaches of the domain may be attributed to the loss of flow, through overspill, along the proximal channel bend. However, as stratification is observed to keep more of the flow in-channel for longer the extent of the stratified flow is greater than that of the unstratified flow, see Figure 5. The importance of this will be discussed in the next section.

### 3.3. Comparison of the Unstratified and Stratified Shallow Water Models

The stratified flow model, Figure 5d, shows a greater flow density in-channel (as much as  $\sim 5 \text{ kgm}^{-3}$ ) than the unstratified model, Figure 5b. This implies that the unstratified model loses more material over-bank than the stratified model. The reduction in over banking in the stratified model means flow is better confined by the channel. For example, the distance at which the in-channel density decreases below  $1018 \text{ kgm}^{-3}$  is reached after  $\sim 10,000 \text{ m}$  along the bend in the stratified model, but is reached after only  $\sim 3500 \text{ m}$  in the unstratified model. Thus, it is seen that stratification of the flow, which enhances densities and thus velocity within channel, results in longer flow runout lengths.

Thus, visual comparison of flow dynamics in Figure 5 shows that the stratified flow exhibits a greater degree of topographic confinement, or channelization, than the unstratified flow, in agreement with the simplified model presented in section 2.3. Here we calculate the root-mean-square error,  $E_r$ , (the root of the mean discrepancy between observed and predicted data squared) in order to quantify the performance of the models. The lower the root-mean-square error the better the agreement between observed and modeled data points.

The root-mean-square error of the flow velocity is smaller using the unstratified,  $E_r=0.2960$ , rather than the stratified,  $E_r=0.3794$ , flow velocity model. This is readily explained in that the unstratified flow model rapidly loses material, through overspilling flow, such that the flow velocity by the end of the main channel is minimal. However, the stratified flow model is well channelized, and eventually dissipates material carried along the channel in a North-Easterly direction, as noted above, across ADCP transects 4–6, see Figure 5c. This causes large errors in the out-of-channel regions of the flow which are (incorrectly) not present in the unstratified model. This is seen by separating error results between the in-channel and out-of-channel regions, see Figure 1. In the stratified flow model the root-mean-square error out-of-channel is  $E_r=0.3988$  whilst it is much smaller in-channel,  $E_r=0.2281$ . Moreover, in the unstratified model the root-mean-square error for in-channel flow is  $E_r=0.3605$ , larger than the stratified flow model.

The root-mean-square error is also calculated for flow density. For this parameter the stratified model,  $E_r=2.544$ , is better than the unstratified model,  $E_r=3.077$ , both in and out-of-channel. This is due to the location of the CTD data points, within or close to the channel, in comparison to the ADCP transects which also cover overbanking flow out-of-channel. It is again seen that the root-mean-square error is considerably reduced in-channel in the stratified model,  $E_r=1.774$ , as compared to the unstratified model,  $E_r=3.004$ .

From comparing the predicted flow dynamics, e.g., velocity and density, against direct field data we have shown that the unstratified shallow water model (Figure 5) poorly captures the dynamics of the observed submarine flow. When employing the vertical stratification model (Figures 5c and 5d) model performance is improved. The effect of stratification is shown in Figure 6 where the difference between the maximum velocity of the stratified and unstratified flow models,

$$\Delta \|u\|_{\max} = \|u\|_{\max, \text{stratified}} - \|u\|_{\max, \text{unstratified}}, \quad (29)$$

and the difference between the stratified and unstratified depth-averaged flow density,

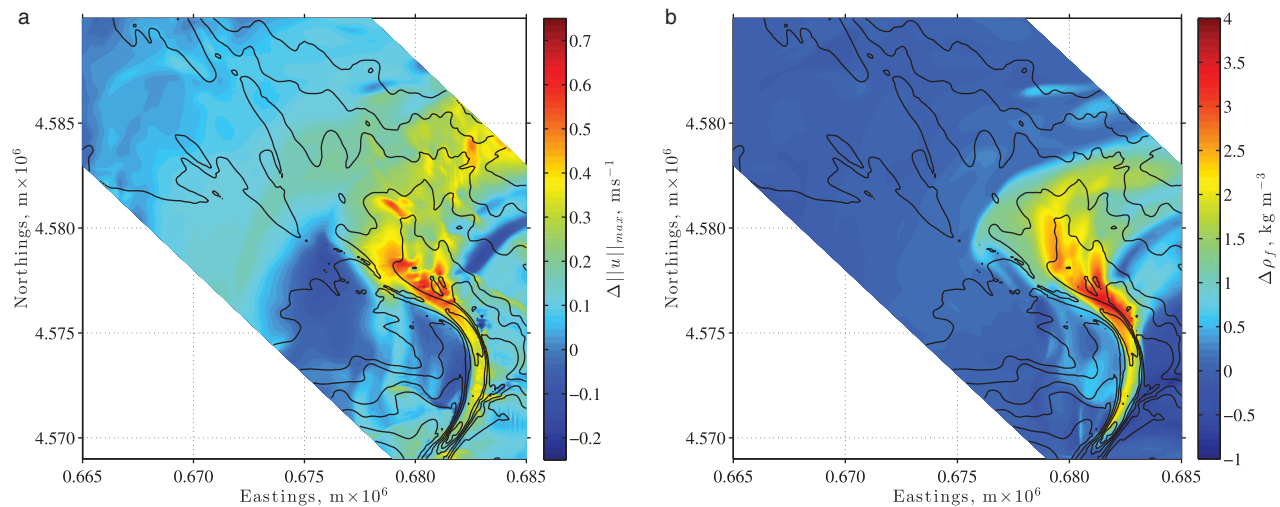


**Figure 6.** The (a) flow velocity, see (29), and (b) density, see (30), difference between the shallow water model assuming stratified and unstratified flow (Figure 5). Plots are displayed in the UTM coordinate system, zone 35 T.

$$\Delta \bar{\rho}_f = \bar{\rho}_f^{\text{stratified}} - \bar{\rho}_f^{\text{unstratified}}, \quad (30)$$

is plotted. Figure 6a highlights that, within the channel, flow-velocity is greater in the stratified model,  $\Delta ||u||_{\max} > 0$ , correspondingly Figure 6b shows that in the stratified model density is greater in the channel,  $\Delta \bar{\rho}_f > 0$ . Moreover, Figure 6b highlights that material is more rapidly lost from within the channel when using the unstratified model, as  $\Delta \bar{\rho}_f < 0$  out-of-channel in the proximal regions of the domain.

The results discussed above indicate that errors are smallest when using the stratified rather than the unstratified model, and errors also decline in-channel as opposed to out-of-channel. The shallow water model should perform better with decreasing aspect ratio,  $\delta$ . Therefore, it is not surprising that the model(s) compare best to the field data in-channel where the observed aspect ratio is an order of magnitude smaller than that out-of-channel, see Appendix B2. This increase in  $\delta$  at the channel edges and in the out-of-channel flow is expected as secondary flow cells and lateral bed gradients may generate strong vertical flow velocities. Moreover, secondary flow cells, omitted from this model, may act to enhance the degree by which flow is constrained by the channel [Kasai *et al.*, 2000; Huijts *et al.*, 2006]. This may explain in part the discrepancy between the predicted and observed degree of channelization of the flow. Long-term variations in flow input conditions not incorporated into these models may affect observed flow dynamics, however long-term studies of the flow suggest it is essentially continuous in nature [Latif *et al.*, 1991]. We also note that the presence of a coastal current, moving obliquely to the gravity current may further account for some of the observed discrepancies. However, recent research has shown that this current does not appear to significantly affect the bulk properties of the gravity current [Sumner *et al.*, 2014]. Therefore, these factors are thought to have only a limited influence on the channelized.

Consequently, the (large) discrepancies between predicted flow dynamics and observations, even for the stratified flow model, indicate that current empirical stratification models do not perform well, see Figure 7. In Figures 7a and 7b the modeled flow stratification is shown to constantly under predict the amount of flow stratification in-channel and out-of-channel, such that the modeled  $W_p$  is greater than observed (Figure 7a). Figure 7b highlights that modeled stratification performs particularly badly in the distal reaches of the domain, where the modeled flow is largely unstratified, whereas the observed flow is highly stratified (Figure 2).

As shown in Figure 4, the consequence of underestimating stratification is that the flow becomes less constrained by its surrounding topography. Therefore, the degree of overspill predicted in the stratified shallow water model is enhanced compared to that observed in real life, see ADCP transects 1–3 in Figures 5a and 5c. In particular this may explain the discrepancy between the model and observed flow in the distal reaches of the system, see Figures 5b and 5d. Here the channel is very shallow, yet the predicted

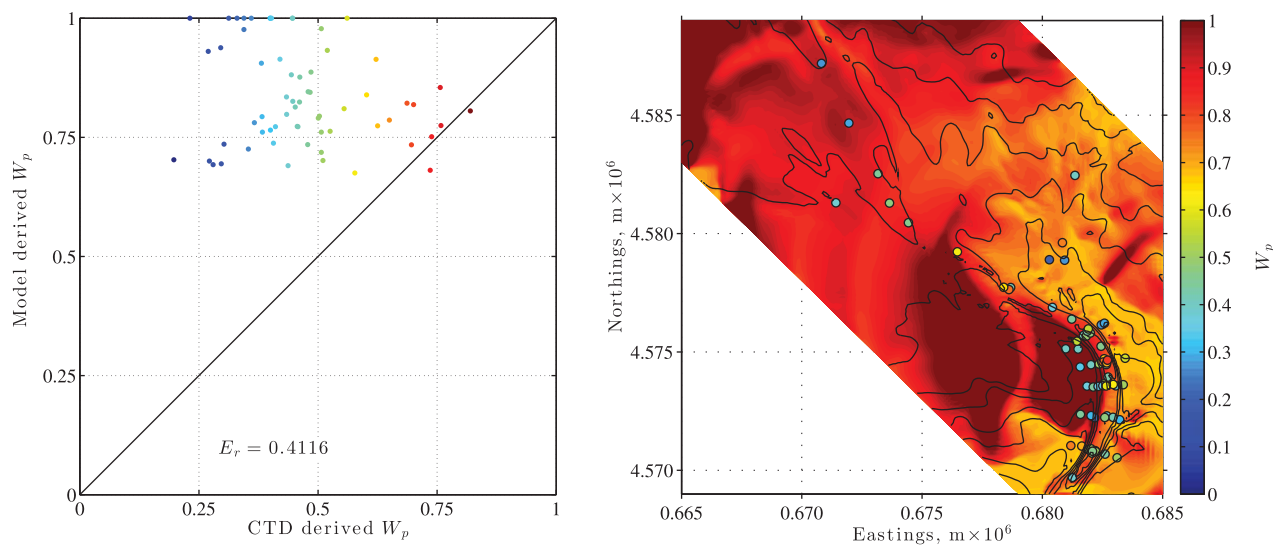


**Figure 7.** (a) Comparison of predicted flow stratification versus CTD-derived flow stratification, point color denotes model-derived  $W_p$  as given in Figure 7b. (b) Predicted flow stratification, for the stratified flow (Figures 5c and 5d), as quantified by the pressure weighting function  $W_p$  (21). Observed flow stratification, derived from CTD data, is denoted by circles.

stratification of the flow is much less than that observed. Thus, the flow predicted by the model is poorly constrained by the bed topography.

#### 4. Discussion

The modeling of flow through the Black Sea submarine channel demonstrates the critical importance of flow stratification in controlling flow overspill, and the maintenance of in channel discharge and velocity. The differences between the flow fields simulated by the unstratified and stratified models were found to be profound, despite the relatively short distances (approximately one bend wavelength) involved in these simulations. This modeling exercise reinforces earlier conceptual models of the role of flow stratification in submarine channels [Hiscott *et al.*, 1997; Peakall *et al.*, 2000a] that have suggested that overspill dominantly involves low-concentration, low-velocity fluid, with consequent limited influence on the main channelized flow [Peakall *et al.*, 2000a, 2000b, 2001]. However, comparison of the model with the Black Sea prototype demonstrates that, even in the stratified case, there is insufficient stratification to cause the modeled flow field to match the observations; thus suggesting that the stratification model utilized here is suboptimal.

The density stratification model (19) used here assumes that there is no variation in stratification in the lower part of the flow. However, the density distributions from the Black Sea, despite this being a predominantly saline-driven gravity current, demonstrate that such a shape function is an over simplification and that there is significant density variation even within the core of the flow, see Figure 2 and Sumner *et al.* [2014]. Moreover, the velocity stratification model used here (14) assumes that for subcritical flows the flow is predominantly vertically uniform, with the flow velocity maximum located within the upper half of the flow. This is contrary to the naïve expectation that a waning flow, of decreasing Froude number, will have increased stratification, with the corresponding velocity maximum located closer toward the bed. The deficiency of the stratification models used here highlights the limitation of scaled experimental models to reproduce the dynamics of real-world scale flows, which may have flow depths and velocities two to three orders of magnitude larger.

How density currents traverse the very large distances of many submarine channels has remained enigmatic for over 125 years [Buchanan, 1887; Daly, 1936]. The runout length of particulate-laden density-driven flows is controlled by two main and interlinked issues: autosuspension and ambient fluid entrainment. Autosuspension is considered a key requirement for particulate flows to travel long distances [Bagnold, 1962; Middleton, 1966; Stacey and Bowen, 1988b], yet the analysis of Parker *et al.* [1986] indicates that this condition only occurs when flows are supercritical. Whilst empirical observations of fluid entrainment show

an approximately quadratic dependence on flow Froude number [Parker *et al.*, 1987], rapid entrainment in supercritical flows will cause them to quickly thicken and slow, with the implication that sediment will then cease to be in a state of autosuspension. This analysis is supported by modeling that suggests that the middle and lower reaches of major submarine channels are subcritical [Bowen *et al.*, 1984; Pirmez and Imran, 2003]. However, if the flow is subcritical and particulate material is not in a state of autosuspension why are the runout length of submarine currents so large? Stacey and Bowen [1988b] suggest a possible solution to this enigma, where they highlight that the criterion for autosuspension, in the basal shear layer of the flow, is aided by a stratified suspension. Here we build on the work of Stacey and Bowen [1988b] and demonstrate that density stratification leads to greater maintenance of in-channel velocity. Furthermore flow stratification also results in low concentration, low density, flow close to the ambient interface. This diffuse flow could very well result in limited mixing at the upper interface, with a consequent reduction in ambient entrainment in comparison to depth-averaged approaches [Peakall *et al.*, 2001] and an associated reduction in downstream momentum loss through overspill. Moreover, following the models of Peakall *et al.* [2000a] and Mohrig and Buttles [2007] which show that flows are typically much deeper than their bounding channels, it is apparent that the flow stripping flux will be dominated by the fluid entrainment flux and thus the rate of dilution of the main channelized part of the flow may be reduced to extremely low levels, further maintaining the autosuspension limit in-channel. Taken together the stratification-induced enhancement of velocity and large-scale reduction of fluid entrainment will enhance the probability of, and longitudinal distance over which, autosuspension will operate. Once autosuspension ceases, flow stratification will act to minimize further energy loss by reducing fluid entrainment to low levels. As a consequence, consideration of flow stratification and its effects may resolve the long runout length enigma of channelized density-driven flows.

So is there evidence for submarine channels exhibiting marked flow stratification throughout their length? Such evidence is provided by the fining upward profiles of submarine channel levees, in turn reflecting the nature of overspill as the levees have progressively increased in relief relative to the channel floor [Hiscott *et al.*, 1997; Klauke *et al.*, 1997; Piper and Deptuck, 1997; Beaubouef, 2004; Dennielou *et al.*, 2006; Kane *et al.*, 2007]. Further evidence is provided by the presence of sandy lobes at the ends of major submarine fans, such as the Amazon and Zaire channels [Damuth and Kumar, 1975; Pirmez *et al.*, 1997; Bonnel, 2005; Jegou *et al.*, 2008]. These channels are amongst the longest known and, in common with other long channels, are very mud-rich systems [Covault *et al.*, 2012]. Thus, there is appreciable sand transported to the very end of channels, in flows that are mud rich. As flow capacity increases with increases in the standard deviation of the grain size of sediment in suspension [Dorrell *et al.*, 2013b], mixed sandy-muddy flows, with a large grain size distribution, are optimal for transporting suspended sediment material and, as flow velocity is dependent on capacity, maintaining autosuspension. Further, whilst the mud-rich component is likely evenly distributed throughout the flow, the sand-rich component is concentrated toward the base [e.g., Hiscott *et al.*, 1997], it is not unreasonable to postulate that significant density stratification is present throughout the length of major submarine channel systems. The modeling results presented herein suggest that it is in part the very presence of this density stratification that enables the maintenance of in-channel velocity and discharge that, in turn, sustains sand grade material transport over distances of many hundreds of kilometers, even across extremely low ( $<0.001$  m/m) gradients [Clark *et al.*, 1992], to the very end of submarine channel systems.

## 5. Conclusions

Novel analytical and numerical models presented herein, and calibrated against three-dimensional field data from subaqueous saline-driven channels on the Black Sea shelf, show that vertical stratification of density-driven flows enhances channelization and increases runout length. The modeling also reveals that current empirical stratification models of gravity currents do not perform well, reflecting in large part the limited stratification that is able to develop in laboratory-scale experiments, and highlighting the limitations of laboratory experiments in capturing the dynamics of real-world flows. The results provide a possible solution to the conundrum of very long runout flows in sediment-driven submarine channel flows. Vertical stratification acts to reduce ambient entrainment, and thus momentum loss, whilst simultaneously increasing the likelihood of the flow being in a state of autosuspension for longer. Such stratified sediment-laden flows

thus provide a mechanism for long runout flows and the associated generation of sandy lobes in the distal reaches of submarine channels.

### Appendix A: Numerical Model

Numerical integration of the nonlinear shallow water model (1–6) is required to yield model solutions. Herein, a high resolution Godunov-type scheme, popular in flow and mass transport modeling [LeVeque, 2002] is used. The high-resolution scheme is based on the well established flux-limiter approach for constructing Total Variation Diminishing (TVD) schemes [Toro, 2009]. The flux-limiting technique ensures high orders of accuracy in smooth regions of the flow, whilst enforcing a TVD property on the flux, enabling efficient shock capturing. The approach used herein follows Delis et al. [2008] who propose and validate the use of a TVD flux model, constructed using a first-order Godunov type flux and a second-order Lax-Wendroff flux, against analytical and experimental results over complex topography.

Before explicitly defining the structure of the numerical model used herein, we first express the shallow water model (1–6) in vector form

$$\frac{\partial \mathbf{V}}{\partial t} + \frac{\partial \mathbf{F}}{\partial x} + \frac{\partial \mathbf{G}}{\partial y} = \mathbf{Q} + \mathbf{R} + \mathbf{S}, \quad \text{where } \mathbf{V} = [h, \bar{\phi}h, \bar{u}h, \bar{v}h, W_p]^T. \quad (\text{A1})$$

Thus, the hydrodynamic evolution of the flow may be determined in terms of the flux vectors  $\mathbf{F}$  and  $\mathbf{G}$ , where from (1) to (6)

$$\mathbf{F} = \left[ \bar{u}h, \bar{u}\bar{\phi}h, \bar{u}^2h + \frac{1}{2}W_p g' \bar{\phi}h^2, \bar{u}\bar{v}h, W_p \right]^T, \quad (\text{A2})$$

$$\mathbf{G} = \left[ \bar{v}h, \bar{v}\bar{\phi}h, \bar{u}\bar{v}h, \bar{v}^2h + \frac{1}{2}W_p g' \bar{\phi}h^2, W_p \right]^T. \quad (\text{A3})$$

Here  $W_p$  is solved explicitly at each time step and each grid cell, using (21) and differentiated with the mean flow variables,  $h, \bar{\phi}, \bar{u}$  and  $\bar{v}$  in the Riemann solver. The remaining weighting terms,  $W_u^2$  and  $W_{u\phi}$ , see Table 2, are treated as dispersive terms in the source terms  $\mathbf{Q}, \mathbf{R}$  and  $\mathbf{S}$  [see e.g., Begnudelli et al., 2010]. Here the dispersive weighting terms,  $W_{u^2}$  and  $W_{u\phi}$ , and diffusive stress terms are described in the vector  $\mathbf{Q}$ , whilst spatial derivatives of the bed topography (corresponding to gravitational forcing on the flow) are described in vector  $\mathbf{R}$ . Following Delis et al. [2008], the source vectors  $\mathbf{Q}$  and  $\mathbf{R}$  are decomposed into vectors incorporating derivatives along the  $x$  axis ( $\mathbf{Q}_F$  and  $\mathbf{R}_F$ ) and  $y$  axis ( $\mathbf{Q}_G$  and  $\mathbf{R}_G$ ),

$$\mathbf{Q} = \mathbf{Q}_F + \mathbf{Q}_G \quad \text{and} \quad \mathbf{R} = \mathbf{R}_F + \mathbf{R}_G. \quad (\text{A4})$$

The summed dispersive and diffusive terms are thus,

$$\mathbf{Q}_F = \frac{\partial}{\partial x} \begin{bmatrix} 0 \\ -(W_{u\phi} - 1)\bar{u}\bar{\phi}h - \overline{D_{px}} \\ -(W_{u^2} - 1)\bar{u}^2h - \frac{h\bar{\tau}_{xx}}{\rho_w} \\ -(W_{u^2} - 1)\bar{u}\bar{v}h - \frac{h\bar{\tau}_{yx}}{\rho_w} \\ 0 \end{bmatrix} \quad \text{and} \quad \mathbf{Q}_G = \frac{\partial}{\partial y} \begin{bmatrix} 0 \\ -(W_{u\phi} - 1)\bar{v}\bar{\phi}h - \overline{D_{py}} \\ -(W_{u^2} - 1)\bar{u}\bar{v}h - \frac{h\bar{\tau}_{xy}}{\rho_w} \\ -(W_{u^2} - 1)\bar{v}^2h - \frac{h\bar{\tau}_{yy}}{\rho_w} \\ 0 \end{bmatrix}, \quad (\text{A5})$$

and the bed gradient terms are

$$\mathbf{R}_F = -g' \bar{\phi}h \frac{\partial}{\partial x} [0, 0, \psi, 0, 0]^T \quad \text{and} \quad \mathbf{R}_G = -g' \bar{\phi}h \frac{\partial}{\partial y} [0, 0, 0, \psi, 0]^T. \quad (\text{A6})$$

The remaining source terms are specified in the vector  $\mathbf{S}$ ,

$$\mathbf{S} = \left[ E \|\bar{u}\|, 0, fh\bar{v} - \frac{\tau_{xz}}{\rho_w}, -fh\bar{u} - \frac{\tau_{yz}}{\rho_w}, 0 \right]^T. \quad (A7)$$

The vectorized form of the shallow water model given above is well suited to numerical integration by finite volume methods [Roe, 1981, 1986], where values of the weighting and diffusive terms in (A5) are calculated explicitly across each grid cell boundary. At a grid cell centered at  $ij$  at time-step  $n$ , discretization of the model, within the wetted domain, takes the following form

$$\mathbf{V}_{ij}^{n+1} - \mathbf{V}_{ij}^n = -\frac{\Delta t^n}{\Delta x} \left( \mathbf{F}_{i+\frac{1}{2}j}^n - \mathbf{F}_{i-\frac{1}{2}j}^n - \mathbf{Q}_{Fij}^n - \mathbf{R}_{Fij}^n \right) \quad (A8)$$

$$-\frac{\Delta t^n}{\Delta y} \left( \mathbf{G}_{i+\frac{1}{2}j}^n - \mathbf{G}_{i-\frac{1}{2}j}^n - \mathbf{Q}_{Gij}^n - \mathbf{R}_{Gij}^n \right) + \Delta t^n S_{ij}^n. \quad (A9)$$

where numerical discretization of the vectors,  $\mathbf{F}_{i\pm\frac{1}{2}j}^n$ ,  $\mathbf{G}_{i\pm\frac{1}{2}j}^n$ ,  $\mathbf{R}_{Fij}^n$  and  $\mathbf{R}_{Gij}^n$  follows the high-resolution TVD scheme proposed by *Delis et al.* [2008], using the superbee flux limiter function [LeVeque, 2002]. The additional diffusive flux vectors,  $\mathbf{Q}_{Fij}^n$  and  $\mathbf{Q}_{Gij}^n$ , are readily discretized following the *Delis et al.* [2008] treatment of the bed gradient terms,  $\mathbf{R}_{Fij}^n$  and  $\mathbf{R}_{Gij}^n$ . Here numerical solutions are sought on a rectilinear mesh, with treatment of cells at solid or open boundaries following the cut-cell approach of *Causon et al.* [2000] and *Ingram et al.* [2003]. Time stepping  $\Delta t^n$  is calculated using the Courant Levy condition, as defined in the two-dimensional, high resolution model of *Delis et al.* [2008], weighted for boundary cells [*Causon et al.*, 2000].

Verification of the above scheme was carried out by comparing against the classical inviscid dambreak problem. A rectilinear channel, constructed at  $25^\circ$  to the rectilinear grid, posed a thorough test of the two-dimensional numerical model. Numerical solutions were collapsed to match analytical solutions, see Figures 8a–8c. The results show grid independence in the model solutions and approximate first-order accuracy, across a shock wave, with decreasing grid cell size, see Figure 8d.

## Appendix B: Density-Driven Channelized Flow in the S.W. Black Sea

A submarine channel system, see Figure 1, was initiated approximately 7.5 ka when a permanent connection was established between the Mediterranean Sea and the Black Sea, via the Strait of Bosphorus [*Flood et al.*, 2009]. Proximally the channel system comprises a single trunk channel up to 1.3 km wide and 25 m deep. Distally the main channel splits into a network of smaller tributary channels [*Flood et al.*, 2009]. The plunging gravity current, formed due to the density difference between Mediterranean and Black Sea water, shows hydrodynamic similarity to deep-sea turbidity currents [*Sumner et al.*, 2014], though we recognize that the Black Sea flow is driven by difference in flow salinity rather than suspended particulate material as in turbidity currents. Water density at the surface of the Black Sea is  $1014 \text{ kgm}^{-3}$  [*Latif et al.*, 1991; *Stanev et al.*, 2004], whereas the surface water density of the Mediterranean Sea is  $1026 \text{ kgm}^{-3}$  [*Millero et al.*, 1978]. This density difference results in an underflow of dense Mediterranean water that passes through the Bosphorous Strait and, on entering the Black Sea, plunges down to form a stratified gravity current, with a dense velocity core overlain by a mixing layer in which flow density tends to that of the ambient Black Sea [*Özsoy et al.*, 2001; *Parsons et al.*, 2010; *Sumner et al.*, 2013, 2014]. The complexity of the seafloor is such that the channel is poorly described by contours of constant depth. However, the bed of the channelized region may be defined by comparison of the local bed depth to a surrounding average bed depth. Here the channel is well described by the region where local bed depth is  $\geq 3 \text{ m}$  deeper than the local average of  $1 \text{ km}^2$  of surrounding topography, as highlighted by the black contour in Figure 1. Flow within this region is denoted as “in-channel,” whilst flow in the remainder of the domain is referred to as “out-of-channel.”

### B1. Field Data Collection

Direct measurements of flow velocity and density of the Black Sea gravity current were obtained from the Black Sea field site using the research vessel *RV Koca Piri Reis* and an autonomous underwater vehicle (AUV), Autosub3, between 19 and 23 May 2010. The velocity of the gravity current was measured in three components using a 1200 KHz Acoustic Doppler Current Profiler (ADCP), with vertical bin sizes of 0.5 m. The ADCP was deployed from Autosub3, enabling transects of velocity data to be collected, capturing the main body

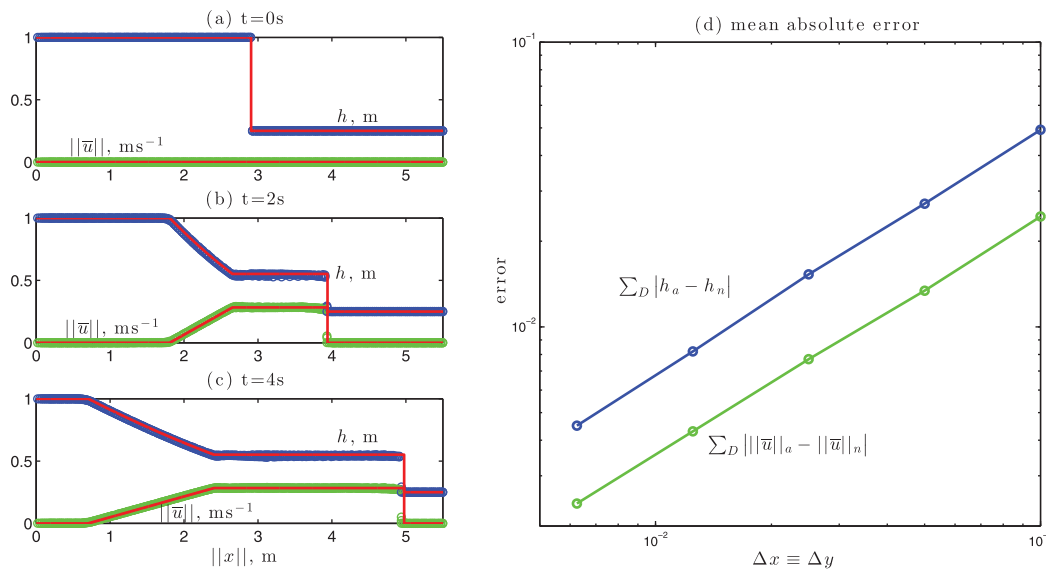


**Figure 8.** Numerical validation of the shallow water model, integrated using the Roe solver proposed by *Delis et al.* [2008] and amended herein to incorporate mass transport of suspended material. Validation compares a lock gate release in a rectangular channel, oriented at  $25^\circ$  to the rectilinear grid, where grid size  $\Delta x = \Delta y = 0.05$  m. (a–c) Flow solutions are plotted at  $t = 0, 1$  and  $2$  s, respectively, where blue circles denote numerical measure of flow depth, green circles flow velocity and red lines denote analytical solutions [see e.g., *Stoker*, 1957]. (d) The approximate first-order grid size-dependent accuracy of the solver, where absolute error is calculated by the sum absolute difference between the analytical (denoted by subscript  $a$ ) and the numerical (denoted by subscript  $n$ ) solutions across the entire domain (denoted subscript  $D$ ) at  $t = 2$  s.

of the flow and horizontal flow velocity maximum, see the *Sumner et al.* [2013, 2014] for further details. The ADCP data presented in this study were collected during a 48 hour Autosub3 mission deployed on 22 May 2010. Due to side-lobe interference from the sea floor [*Simpson*, 1986; *Gordon*, 1996] and topographic constraints, limiting the height above the seabed which the Autosub3 could be safely deployed, the ADCP transects only resolved flow velocity to within a few meters of the sea bed. Further, the flow – ambient fluid interface was not always captured. Therefore, we use the flow velocity maximum, henceforth denoted by  $||u||_{\max}$ , to represent inertial processes because it was clearly imaged. This avoids the addition of unquantifiable errors to flow velocity data which would arise by extrapolating to estimate the depth averaged velocity.

Vertical salinity profiles were measured by deploying a conductivity temperature depth probe (CTD) from the stationary research vessel (*RV Koca Piri Reis*). For consistency with the theoretical model, flow density is readily derived from the CTD data following (7). It was assumed that at the flow-ambient fluid interface the excess density of the flow vanished (19), following the density stratification model of *Abad et al.* [2011]. Therefore, depth averaged densities, derived from the CTD probe, were computed between the flow bed and the depth where the CTD-derived density was equal to  $1014 \text{ kg m}^{-3}$ . Grab samples were taken along the sea bed of the channel, see Figure 1. Wet sieving, drying and weighing of these samples show an approximate median grain size of  $d_{50} = 250 \mu\text{m}$ .

## B2. The Shallow Water Assumption: Direct Field Analysis of Flow Aspect Ratio

The hydrostatic pressure field assumption of standard shallow water models is based on the assumption that vertical length scales,  $h$ , are small in comparison to horizontal length scales,  $L$ , and as such the aspect ratio of the flow,  $\delta = h/L \ll 1$ . Applying this assumption to the fluid mass conservation equation (1) one finds that the ratio of the magnitude of the vertical flow velocity,  $w$ , to horizontal flow velocity must also scale with  $\delta$

$$\delta = \mathcal{O}\left(\frac{|\bar{w}|}{|\bar{u}|}\right). \quad (\text{B1})$$

Thus, the ratio of vertical to horizontal flow speed is indicative of the aspect ratio of the flow, see Table 1.

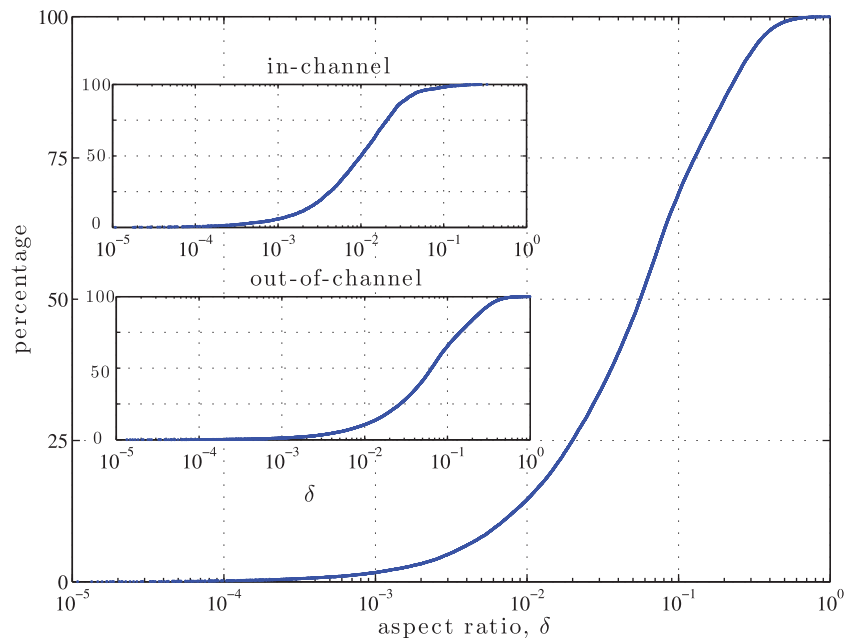


**Figure 9.** Cumulative distribution plot of the flow aspect ratio in the channelized submarine flow in the S.W. Black Sea. The flow aspect ratio is derived from ratio of depth averaged vertical to horizontal flow velocity,  $\delta \approx w/|u|$ , calculated at the depth of the maximum downstream flow velocity, see Appendix B2. Also plotted is the distribution of the in-channel and out-of-channel aspect ratio.

In Figure 9 the flow aspect ratio, as quantified by the ratio of vertical to horizontal flow velocity (40), is plotted, with an average flow aspect ratio of  $\delta = \mathcal{O}(10^{-1})$ . From Figure 9 it is noted that the flow aspect ratio in-channel is smaller than out-of-channel. The aspect ratio of the flow within the channel is small due to the high-density fluid generating strong downstream flow velocity, where there is negligible change in bed gradient (see e.g., Figure 5). The increase in the magnitude of the flow aspect ratio out-of-channel, see Figure 9, is caused when the ratio of vertical velocity to horizontal velocity increases. Vertical velocities may increase due to flow over banking on the channel sidewalls or interaction with bed forms. Moreover, out-of-channel, horizontal flow velocity will wane as flow density decreases, see for example, Figure 5. The variation in aspect ratio between in-channel and out-of-channel is suggestive that the shallow water model (1–6) will perform better within the channel, whereas strong vertical velocities out-of-channel may generate inaccuracies in the model.

**Notation**

- $\alpha$  latitude.
- $\delta$  aspect ratio.
- $\zeta_1$  velocity Structure function.
- $\zeta_2$  density Structure function.
- $\eta$  dimensionless depth.
- $\nu_t$  eddy viscosity.
- $\rho_{f,w,s}$  density of flow, ambient fluid, material transported.
- $\tau_{ij}$  shear stress.
- $\sigma_t$  Schmidt number.
- $\phi$  dimensionless excess density.
- $\psi$  bed depth.
- $\omega$  rotation rate.
- $C_z$  chezy drag coefficient.
- $D_{pi}$  transported material diffusion.
- $E$  entrainment rate of ambient fluid.

$f$	Coriolis force.
$Fr_d$	densimetric Froude number.
$g'$	reduced gravity.
$h$	flow depth.
$K$	eddy diffusivity.
$P$	pressure.
$u, v, w$	flow velocity.
$  u  $	summed horizontal velocity.
$W_{u\phi}$	convective transport weighting term.
$W_{u^2}$	convective acceleration weighting term.
$W_p$	hydrostatic pressure weighting term.
$x, y, z$	spatial coordinates.

### Acknowledgments

This research was supported by awards NE/F020511/1, NE/F020120/1 and NE/F020279/1 from the Natural Environmental Research Council (NERC) we acknowledge the University of Hull for funding gold open access for this paper. Further, we thank Rick Hiscott and Ali Aksu of Memorial University, Canada, Roger Flood of Stony Brook University, USA and Dogan Yasar of Dokuz Eylül University, Turkey, along with the Master and crew of the *RV Koca Piri Reis* for their assistance with cruise planning and operation.

### References

- Abad, J. D., O. E. Sequeiros, B. Spinewine, C. Pirmez, M. H. Garcia, and G. Parker (2011), Secondary current of saline underflow in a highly meandering channel: Experiments and theory, *J. Sediment. Res.*, *81*, 787–813.
- Abd El-Gawad, S., A. Cantelli, C. Pirmez, D. Minisini, Z. Sylvester, and J. Imran (2012), Three-dimensional numerical simulation of turbidity currents in a submarine channel on the seafloor of the Niger Delta slope, *J. Geophys. Res.*, *117*, C05026, doi:10.1029/2011JC007538.
- Amy, L., J. Peakall, and P. Talling (2005), Density- and viscosity-stratified gravity currents: Insight from laboratory experiments and implications for submarine flow deposits, *Sediment. Geol.*, *179*(1), 5–29.
- Arnott, R. W. C. (2007), Stratal architecture and origin of lateral accretion deposits (LADs) and conterminous inner-bank levee deposits in a base-of-slope sinuous channel, lower Isaac Formation (Neoproterozoic), East-Central British Columbia, Canada, *Mar. Pet. Geol.*, *24*(6), 515–528.
- Bagnold, R. (1962), Auto-suspension of transported sediment; turbidity currents, *Proc. R. Soc. London, Ser. A*, *265*(1322), 315–319.
- Beaubouef, R. T. (2004), Deep-water leveed-channel complexes of the Cerro Toro Formation, Upper Cretaceous, southern Chile, *AAPG Bull.*, *88*(11), 1471–1500.
- Begnudelli, L., A. Valiani, and B. F. Sanders (2010), A balanced treatment of secondary currents, turbulence and dispersion in a depth-integrated hydrodynamic and bed deformation model for channel bends, *Adv. Water Resour.*, *33*(1), 17–33.
- Bonnel, C. (2005), Mise en place des lobes distaux dans les systèmes turbiditiques actuels: Analyse comparée des systèmes du Zaïre, Var et Rhône. PhD thesis, Univ. Bordeaux, Bordeaux.
- Bowen, A. J., W. R. Normark, and D. J. W. Piper (1984), Modelling of turbidity currents on Navy submarine fan, California Continental Borderland, *Sedimentology*, *31*, 169–185.
- Buchanan, J. Y. (1887), On the land slopes separating continents and ocean basins, especially those on the west coast of Africa: Observed and surveyed in the SS “Buccaneer”, belonging to the India-Rubber, Gutta-Percha, and telegraph works company (limited) of Silvertown, *Scott. Geogr. Mag.*, *3*(5) 217–238.
- Castro Díaz, M. J., E. D. Fernández-Nieto, T. Morales de Luna, G. Narbona-Reina, and C. Parés (2013), A HLLC scheme for nonconservative hyperbolic problems. Application to turbidity currents with sediment transport, *ESAIM: Math. Modell. Numer. Anal.*, *47*, 1–32, doi:10.1051/m2an/2012017.
- Causon, D. M., D. M. Ingram, G. C. Mingham, G. Yang, and R. V. Pearson (2000), Calculation of shallow water flows using a Cartesian cut cell approach, *Adv. Water Resour.*, *23*(5), 545–562.
- Chemetsky, A. S., H. M. Schuttelaars, and S. A. Talke (2010), The effect of tidal asymmetry and temporal settling lag on sediment trapping in tidal estuaries, *Ocean Dyn.*, *60*(5), 1219–1241.
- Chough, S. K., and R. Hesse (1980), The Northwest Atlantic Mid-Ocean Channel of the Labrador Sea; III, Head spill vs. body spill deposits from turbidity currents on natural levees, *J. Sediment. Res.*, *50*(1), 227–234.
- Christoffersen, J. B., and I. G. Jonsson (1985), Bed friction and dissipation in a combined current and wave motion, *Ocean Eng.*, *12*(5), 387–423.
- Clark, J. D., N. H. Kenyon, and K. T. Pickering (1992), Quantitative analysis of the geometry of submarine channels: Implications for the classification of submarine fans, *Geology*, *20*(7), 633–636.
- Covault, J. A., E. Shelef, M. Traer, S. M. Hubbard, B. W. Romans, and A. Fildani (2012), Deep-water channel run-out length: Insights from seafloor geomorphology, *J. Sediment. Res.*, *82*(1), 25–40.
- Daly, R. A. (1936), Origin of submarine canyons, *Am. J. Sci.*, *31*, 401–420.
- Damuth, J. E., and N. Kumar (1975), Amazon cone: Morphology, sediments, age and growth pattern, *Geol. Soc. Am.*, *86*, 863–878.
- Das, H. S., J. Imran, C. Pirmez, and D. Mohrig (2004), Numerical modeling of flow and bed evolution in meandering submarine channels, *J. Geophys. Res.*, *109*, C10009, doi:10.1029/2002JC001518.
- Delis, A. I., M. Kazolea, and N. A. Kampanis (2008), A robust high-resolution finite volume scheme for the simulation of long waves over complex domains, *Int. J. Numer. Methods Fluids*, *56*(4), 419–452, doi:10.1002/flid.1537.
- Dennielou, B., A. Huchon, C. Beaudouin, and S. Berné (2006), Vertical grain-size variability within a turbidite levee: Autocyclicity or allocyclicity? A case study from the Rhône neofan, Gulf of Lions, Western Mediterranean, *Mar. Geol.*, *234*(1), 191–234.
- Dorrell, R. M., and A. J. Hogg (2012), Length and time scales of response of sediment suspensions to changing flow conditions, *J. Hydraul. Eng.*, *138*(5), 430–439.
- Dorrell, R. M., S. E. Darby, J. Peakall, E. J. Sumner, D. R. Parsons, and R. B. Wynn (2013a), Superelevation and overspill control secondary flow dynamics in submarine channels, *J. Geophys. Res. Oceans*, *118*, 3895–3915, doi:10.1002/jgrc.20277.
- Dorrell, R. M., A. J. Hogg, and D. Pritchard (2013b), Polydisperse suspensions: Erosion, deposition, and flow capacity, *J. Geophys. Res. Earth Surface*, *118*, 1–17, doi:10.1002/jgrf.20129.
- Dyer, K., and R. Soulsby (1988), Sand transport on the continental shelf, *Annu. Rev. Fluid Mech.*, *20*, 295–324.

- Ellison, T., and J. Turner (1959), Turbulent entrainment in stratified flows, *J. Fluid Mech.*, *6*(03), 423–448.
- Engelund, F. (1974), Flow and bed topography in channel bends, *J. Hydraul. Div. Am. Soc. Civ. Eng.*, *100*(11), 1631–1648.
- Ezz, H., and J. Imran (2014), Curvature-induced secondary flow in submarine channels, *Environ. Fluid Mech.*, *14*, 343–370, doi:10.1007/s10652-014-9345-4.
- Felix, M. (2002), Flow structure of turbidity currents, *Sedimentology*, *49*(3), 397–419.
- Felix, M., S. Sturton, and J. Peakall (2005), Combined measurements of velocity and concentration in experimental turbidity currents, *Sediment. Geol.*, *179*(1), 31–47.
- Flood, R. D., R. N. Hiscott, and A. E. Aksu (2009), Morphology and evolution of an anastomosed channel network where saline underflow enters the Black Sea, *Sedimentology*, *56*(3), 807–839.
- Garcia, M., and G. Parker (1993), Experiments on the entrainment of sediment into suspension by a dense bottom current, *J. Geophys. Res.*, *98*(C3), 4793–4807, doi:10.1029/92JC02404.
- Giorgio Serchi, F., J. Peakall, D. B. Ingham, and A. D. Burns (2011), A unifying computational fluid dynamics investigation on the river-like to river-reversed secondary circulation in submarine channel bends, *J. Geophys. Res.*, *116*, C06012, doi:10.1029/2010JC006361.
- Gordon, L. (1996), *Acoustic Doppler Current Profilers Principles of Operation: A Practical Primer*, RD Instrum. Ltd, San Diego, Calif.
- Hesse, R., S. K. Chough, and A. Rakofsky (1987), The Northwest Atlantic Mid-Ocean Channel of the Labrador Sea. V. Sedimentology of a giant deep-sea channel, *Can. J. Earth Sci.*, *24*, 1595–1624.
- Hiscott, R. N., F. R. Hall, and C. Pirmez (1997), Turbidity-current overspill from the Amazon Channel: Texture of the silt/sand load, paleoflow from anisotropy of magnetic susceptibility, and implications for flow processes, *Proc. Ocean Drill. Program Sci. Results*, *155*, 53–78.
- Hogg, A. J., and D. Pritchard (2004), The effects of hydraulic resistance on dam-break and other shallow inertial flows, *J. Fluid Mech.*, *501*, 179–212.
- Hu, P., Z. Cao, G. Pender, and G. Tan (2012), Numerical modelling of turbidity currents in the Xiaolangdi reservoir, Yellow river, China, *J. Hydrol.*, *464–465*, 41–53, doi:10.1016/j.jhydrol.2012.06.032.
- Huijts, K. M. H., H. M. Schuttelaars, H. E. de Swart, and A. Valle-Levinson (2006), Lateral entrapment of sediment in tidal estuaries: An idealized model study, *J. Geophys. Res.*, *111*, C12016, doi:10.1029/2006JC003615.
- Hutter, K., and Y. Nohguchi (1990), Similarity solutions for a Voellmy model of snow avalanches with finite mass, *Acta Mech.*, *82*(1), 99–127.
- Imran, J., A. Kassem, and S. Khan (2004), Three-dimensional modeling of density current. I. Flow in straight confined and unconfined channels, *J. Hydraul. Res.*, *42*(6), 578–590.
- Ingram, D. M., D. M. Causon, and C. G. Mingham (2003), Developments in Cartesian cut cell methods, *Math. Comput. Simul.*, *61*(3–6), 561–572.
- Islam, M. A., and J. Imran (2010), Vertical structure of continuous release saline and turbidity currents, *J. Geophys. Res.*, *115*, C08025, doi:10.1029/2009JC005365.
- Jegou, I., B. Savoye, C. Pirmez and L. Droz (2008), Channel-mouth lobe complex of the recent Amazon Fan: The missing piece, *Mar. Geol.*, *252*, 62–77.
- Kane, I. A., B. C. Kneller, M. Dykstra, A. Kassem, and W. McCaffrey (2007), Anatomy of a submarine channel-levee: An example from Upper Cretaceous slope sediments, Rosario Formation, Baja California, Mexico, *Mar. Pet. Geol.*, *24*(6), 540–563.
- Kasai, A., A. E. Hill, T. Fujiwara, and J. H. Simpson (2000), Effect of the Earth's rotation on the circulation in regions of freshwater influence, *J. Geophys. Res.*, *105*(7), 16,961–16,969.
- Kassem, A., and J. Imran (2004), Three-dimensional modeling of density current. II. Flow in sinuous confined and unconfined channels, *J. Hydraul. Res.*, *42*(6), 591–602.
- Keevil, G., J. Peakall, J. L. Best, and K. J. Amos (2006), Flow structure in sinuous submarine channels: Velocity and turbulence structure of an experimental submarine channel, *Mar. Geol.*, *229*(3), 241–257.
- Keevil, G., J. Peakall, and J. L. Best (2007), The influence of scale, slope and channel geometry on the flow dynamics of submarine channels, *Mar. Pet. Geol.*, *24*(6–9), 487–503.
- Khripounoff, A., A. Vangriesheim, N. Babonneau, P. Crassous, B. Dennielou, and B. Savoye (2003), Direct observation of intense turbidity current activity in the Zaire submarine valley at 4000 m water depth, *Mar. Geol.*, *194*(3–4), 151–158.
- Klaucke, I., R. Hesse and W. B. F. Ryan (1997), Flow parameters of turbidity currents in a low-sinuosity giant deep-sea channel currents, *Sedimentology*, *44*(6), 1093–1102.
- Kostic, S., and G. Parker (2006), The response of turbidity currents to a canyonfan transition: Internal hydraulic jumps and depositional signatures, *J. Hydraul. Res.*, *44*, 631–653, doi:10.1080/00221686.2006.9521713.
- Latif, M. A., E. Özsoy, T. Oguz, and Ü. Ünlüata (1991), Observations of the Mediterranean inflow into the Black Sea, *Deep Sea Res., Part A*, *38*, S711–S723.
- LeVeque, R. (2002), *Finite Volume Methods for Hyperbolic Problems*, Cambridge Univ. Press, Cambridge, U. K.
- Middleton, G. (1966), Small-scale models of turbidity currents and the criterion for auto-suspension, *J. Sediment. Res.*, *36*(1), 202–208.
- Migeon, S., T. Mulder, B. Savoye, and F. Sage (2012), Hydrodynamic processes, velocity structure and stratification in natural turbidity currents: Results inferred from field data in the Var Turbidite System, *Sediment. Geol.*, *245*, 48–62.
- Millero, F. J., D. Means, and C. Miller (1978), The densities of Mediterranean sea waters, *Deep Sea Res.*, *25*(6), 563–569.
- Mohrig, D., and J. Buttles (2007), Deep turbidity currents in shallow channels, *Geology*, *35*(2), 155–158.
- Mulder, T., B. Savoye, and J. P. M. Syvitski (1997), Numerical modelling of a mid-sized gravity flow: The 1979 Nice turbidity current (dynamics, processes, sediment budget and seafloor impact), *Sedimentology*, *44*(2), 305–326.
- Özsoy, E., M. Latif, S. Tugrul, and Ü. Ünlüata (1995), Exchanges with the Mediterranean, fluxes, and boundary mixing processes in the Black Sea, *Bull. Inst. Océanographique*, pp. 1–25.
- Özsoy, E., D. Di Iorio, M. Gregg, and J. Backhaus (2001), Mixing in the Bosphorus Strait and the Black Sea continental shelf: Observations and a model of the dense water outflow, *J. Mar. Syst.*, *31*(1–3), 99–135.
- Parker, G., Y. Fukushima, and H. Pantin (1986), Self-accelerating turbidity currents, *J. Fluid Mech.*, *171*, 145–181.
- Parker, G., M. Garcia, Y. Fukushima, and W. Yu (1987), Experiments on turbidity currents over an erodible bed, *J. Hydraul. Res.*, *25*(1), 123–147.
- Parsons, D. R., J. Peakall, A. E. Aksu, R. D. Flood, R. N. Hiscott, Ş. Beşiktepe, and D. Moulard (2010), Gravity-driven flow in a submarine channel bend: Direct field evidence of helical flow reversal, *Geology*, *38*(12), 1063–1066.
- Parsons, J. D., C. T. Friedrichs, P. A. Traykovski, D. Mohrig, J. Imran, J. P. Syvitski, G. Parker, P. Puig, J. L. Buttles, and M. H. Garcia (2009), The mechanics of marine sediment gravity flows, in *Continental Margin Sedimentation: From Sediment Transport to Sequence Stratigraphy*, edited by C. A. Nittrouer et al., pp. 275–337, Blackwell, Oxford, U. K.
- Peakall, J., B. McCaffrey, and B.C. Kneller (2000a), A process model for the evolution, morphology, and architecture of sinuous submarine channels, *J. Sediment. Res.*, *70*(3), 434–448.

- Peakall, J., W. D. McCaffrey, B. C. Kneller, C. E. Stelling, T. R. McHargue, and W. J. Schweller (2000b), A process model for the evolution of submarine fan channels: Implications for sedimentary architecture, in *Fine-Grained Turbidite Systems*, AAPG Mem. 72/SEPM Spec. Publ. 68, edited by A. H. Bouma and C. G. Stone, pp. 73–88, SEPM, Okla.
- Peakall, J., M. Felix, B. McCaffrey, and B. C. Kneller (2001), Particulate gravity currents: Perspectives, in *Particulate Gravity Currents*, vol. 16 (Special Publication 31 of the IAS), edited by W. D. McCaffrey et al., pp. 1–8, Wiley-Blackwell, U. K.
- Piper, D. J. W., and M. Deptuck (1997), Fine-grained turbidites of the Amazon Fan: Facies characterization and interpretation, *Proc. Ocean Drill. Program Sci. Results*, 155, 79108.
- Pirmez, C., and J. Imran (2003), Reconstruction of turbidity currents in Amazon Channel, *Mar. Pet. Geol.*, 20(6), 823–849.
- Pirmez, C., R. N. Hiscott, and J. D. Kronen (1997), Sandy turbidite successions at the base of channel-levee systems of the Amazon Fan revealed by FMS logs and cores: Unraveling the facies architecture of large submarine fans, *Proc. Ocean Drill. Program Sci. Results*, 155, 7–33.
- Roe, P. (1981), Approximate Riemann solvers, parameter vectors, and difference schemes, *J. Comput. Phys.*, 43(2), 357–372.
- Roe, P. (1986), Characteristic-based schemes for the Euler equations, *Annu. Rev. Fluid Mech.*, 18(1), 337–365.
- Sequeiros, O. E., B. Spinewine, R. Beauouef, T. Sun, M. Garcia, and G. Parker (2010), Characteristics of velocity and excess density profiles of saline underflows and turbidity currents flowing over a mobile bed, *J. Hydraul. Eng.*, 136, 412–433.
- Simpson, M. R. (1986), Evaluation of a vessel-mounted acoustic Doppler current profiler for use in rivers and estuaries, in *Proceedings 3rd Working Conference on Current Measurement*, 3, 106–121, Institute of Electrical and Electronics Engineers, Washington, D. C., doi:10.1109/CCM.1986.1158482.
- Soulsby, R. (1997), *Dynamics of Marine Sands, a Manual for Practical Applications*, Thomas Telford, London.
- Stacey, M. W., and A. J. Bowen (1988a), The vertical structure of density and turbidity currents: Theory and observations, *J. Geophys. Res.*, 93(C4), 3528–3542.
- Stacey, M. W., and A. J. Bowen (1988b), The vertical structure of turbidity currents and a necessary condition for self-maintenance, *J. Geophys. Res.*, 93(C4), 3543–3553.
- Stanev, E. V., J. Staneva, J. L. Bullister, and J. W. Murray (2004), Ventilation of the Black Sea pycnocline. Parameterization of convection, numerical simulations and validations against observed chlorofluorocarbon data, *Deep Sea Res., Part I*, 51(12), 2137–2169.
- Stoker, J. J. (1957), *Water Waves: The Mathematical Theory With Applications*, Intersci. Publ., N. Y.
- Sumner, E. J., J. Peakall, D. R. Parsons, R. B. Wynn, S. E. Darby, R. M. Dorrell, S. D. McPhail, J. Perrett, A. Webb, and D. White (2013), First direct measurements of hydraulic jumps in an active submarine density current, *Geophys. Res. Lett.*, 40, 5904–5908, doi:10.1002/2013GL057862.
- Sumner, E. J., J. Peakall, R. M. Dorrell, D. R. Parsons, R. B. Wynn, S. E. Darby, S. D. McPhail, J. Perrett, A. Webb, and D. White (2014), Driven around the bend: Spatial evolution and controls on the orientation of helical bend flow in a natural submarine gravity current, *J. Geophys. Res. Oceans*, 119, 898–913, doi:10.1002/2013JC009008.
- Tan, W.-Y. (1992), *Shallow Water Hydrodynamics: Mathematical Theory and Numerical Solution for a Two-Dimensional System of Shallow-Water Equations*, Elsevier, Water and Power Press, Beijing, China.
- Toro, E. (2009), *Riemann Solvers and Numerical Methods for Fluid Dynamics: A Practical Introduction*, Springer, Berlin.
- Ünlülata, Ü., T. Oğuz, M. Latif, and E. Özsoy (1990), On the physical oceanography of the Turkish Straits, in *The Physical Oceanography of Sea Straits*, edited by L. J. Pratt, pp. 25–60, Springer, Netherlands.
- Vangriesheim, A., A. Khripounoff, and P. Crassous (2009), Turbidity events observed in situ along the Congo submarine channel, *Deep Sea Res., Part II*, 56(23), 2208–2222.
- Wei, T., J. Peakall, D. R. Parsons, Z. Chen, B. Zhao, and J. Best (2013), Three-dimensional gravity-current flow within a subaqueous bend: Spatial evolution and force balance variations, *Sedimentology*, 60, 1668–1680, doi:10.1111/sed.12052.
- Wu, W. (2004), Depth-averaged two-dimensional numerical modeling of unsteady flow and nonuniform sediment transport in open channels, *J. Hydraul. Eng.*, 130, 1013–1024.
- Yeh, T., M. Cantero, A. Cantelli, C. Pirmez and G. Parker (2013), Turbidity current with a roof: Success and failure of RANS modeling for turbidity currents under strongly stratified conditions, *J. Geophys. Res. Earth Surf.*, 118, 1975–1998, doi:10.1002/jgrf.20126.
- Zeng, J., and D. R. Lowe (2006), Numerical simulation of turbidity current flow and sedimentation: I. theory, *Sedimentology*, 44(1), 67–84.